Modeling the dynamics of dense pyroclastic flows on Venus: insights into pyroclastic eruptions

I. Ganesh[1], L. A. McGuire[2], and L. M. Carter[1]

[1] Department of Planetary Sciences, University of Arizona.

[2] Department of Geosciences, University of Arizona.

Corresponding author: Indujaa Ganesh (indujaa@email.arizona.edu)

Key Points:

- Pyroclastic flows from small, low-energy eruptions are capable of emplacing some of the proposed pyroclastic deposits on Venus.
- Multiple episodes of explosive activity distributed in space and time are required.
- Gentle slopes < 2° at the deposit locations indicate emplacement by highly fluidized flows.

Abstract

On Venus, relatively young deposits near volcanic and coronal summits with unique radar characteristics have been proposed to be emplaced by pyroclastic density currents (PDCs). The proposed units are laterally extensive, long-runout deposits showing moderate to high radar backscatter and circular polarization ratio in 12.6 cm wavelength synthetic aperture radar data. Previous studies have hypothesized that a recent resumption in volcanism activity in the form of PDC-forming eruptions could have emplaced these deposits. We model the dynamics of dense PDCs using a 2D, depth-averaged framework focusing on regions where stereo-derived topography coverage is available; this includes the flanks of Irnini Mons, Anala Mons, Didilia Corona and Pavlova Corona. Two different mechanisms of initiation— impulsive collapse of an eruption column and sustained pyroclastic fountaining — are considered. The results emphasize the importance of pyroclastic flow fluidization via high pore pressure in emplacing long-runout deposits along gently sloping (< 2°) volcanic flanks. We also show that collapse of columns >1.2 – 1.4 km tall as well as pyroclastic fountains lasting >400 s with fountain heights of 50 m are capable of generating pyroclastic flows that could emplace some of the smaller deposits studied. For the large deposits at Irnini Mons, more energetic flows resulting from taller column heights would be necessary; the dynamics of such flows under Venus's conditions are not well understood. Distinguishing between the two initiation styles — column collapse and sustained fountaining — is not feasible with currently available datasets and would require higher resolution imagery and topography data.

Plain Language Summary

High atmospheric pressure and density on Venus prevent the formation of steady, convective volcanic plumes associated with explosive activity. Instead, volcanic eruption columns are expected to collapse, feeding hot and flowing mixtures of torn-apart magma and gases termed as pyroclastic density currents (PDCs). Many researchers have previously identified possible deposits of PDCs near large volcanoes and coronae features using radar data. These deposits are comparable in size to some of the ancient PDC deposits on Earth not known to form in current times. How such features form and get deposited across a large area on Venus is still not clearly known. To understand some of the issues related to PDC transport and emplacement (such as the flow distance, velocity and volume, and vent conditions), we model PDC flow under Venus's

ambient settings. Our model results show that small-scale eruptions could have formed some of the previously identified PDC deposits on Venus. The PDCs would have been highly fluidized to form large deposits on Venus's sub-horizontal landscape. Our models do not recreate the larger deposits well, indicating formation by energetic PDCs. Higher resolution data of Venus's surface could help refine the model and engage in more detailed studies of these deposits.

1 Introduction

The surface of Venus is dominated by volcanic landscapes such as lava channels, lava flows, flood lavas, shield fields, domes, calderas and so on (Head *et al.*, 1991, 1992). The morphology of many of these features, with the exception of some steep-sided domes (McKenzie *et al.*, 1992; Fink *et al.*, 1993), is suggestive of effusive activity involving low-viscosity magmas (Campbell and Campbell, 1992; Head *et al.*, 1992). The prevalence of effusive activity was also signified by the identification of rocks with alkaline gabbroid and oceanic basaltic compositions at the landing sites of Venera 13 and 14, respectively (Surkov *et al.*, 1983, 1984). Explosive activity is predicted to be less common on Venus due to reduction in volatile exsolution from magmas brought about by the high atmospheric pressure (Head and Wilson, 1982; Wilson and Head, 1983). Only a few signs of volatile-rich pyroclastic activity have been identified in the 12.6 cm wavelength synthetic aperture radar (SAR) data from the Magellan mission and the ground-based Arecibo Observatory (Keddie and Head, 1995; McGill, 2000; Campbell and Clark, 2006; Grosfils *et al.*, 2011; Ghail and Wilson, 2015). These include volcanic and coronal summit deposits characterized by high radar echoes (bright appearance) in both Magellan and Arecibo SAR datasets. The proposed pyroclastic deposits have diffuse margins that expose underlying features, and lack definitive flow texture in the interior (McGill, 2000; Campbell and Clark, 2006; Grosfils *et al.*, 2011). They show high circular polarization ratio (CPR) values in the Arecibo polarimetry measurements, interpreted to be caused by extensively distributed centimeter sized clasts within the deposit (Campbell *et al.*, 2017). Many of these units appear to have been emplaced radially outward from summit calderas or annular boundaries of coronae along very gentle slopes (<2°). The extent of continuous bright material from the summit to the deposit terminus ranges from 40 – 120 km at different locations. Source vents for these deposits have not been identified, due to either vent sizes being smaller than the resolution of the SAR dataset (Campbell *et al.*, 2017) or vents being buried after the eruption (Grosfils *et al.*, 2011).

Further investigations into the origin of these deposits are of interest because of the implications for higher volatile content in Venus's interior. Given their position in local stratigraphy, these deposits likely represent recent (or even ongoing) pyroclastic eruptions from volatile-rich magma reservoirs (Campbell *et al.*, 2017). Hence, studies of these deposits can help in identifying regions of young volcanism, volatile-rich magmas, or evolved rock compositions on Venus.

A key question regarding the long runout pyroclastic deposits on Venus's surface is the mechanism by which they were emplaced. Previous studies have hypothesized that the observed deposits were emplaced by pyroclastic density currents (PDCs) resulting from a collapsing eruption column rather than a Plinian style ashfall (Moore, Plaut, *et al.*, 1992; Moore, Schenk, *et al.*, 1992; Campbell, 1994; Keddie and Head, 1995; Ghail and Wilson, 2015). This is due to two reasons. Firstly, bubble nucleation in the magma begins at shallower depths than on Earth, resulting in lesser gas expansion preceding magma fragmentation (Garvin *et al.*, 1982; Head and Wilson, 1982, 1986). Consequently, lower ejection velocity and higher pyroclast density relative to eruptions on Earth are expected (Head and Wilson, 1986). Secondly, eruption columns forming at or below the mean planetary radius (MPR) at low latitudes on Venus are subjected to higher ambient pressure and density conditions which drive the column towards gravitational collapse (Wilson and Head, 1983; Glaze, 1999; Airey *et al.*, 2015). The sharp decline in atmospheric pressure with increasing altitude could allow plumes released at higher altitudes to rise to heights greater than 40 km (Esposito, 1984; Glaze, 1999). Additionally, studies of magma ascent have shown that >3 wt% H_2O, >4 wt% CO_2 (Head and Wilson, 1982) or > 3 wt% H_2O mixed with 3 wt% CO_2 (Airey *et al.*, 2015) is needed to cause explosive disruption of magma at the MPR; whereas, only ~ 2 wt% H_2O is required for explosive eruptions to occur at several kilometers above the MPR (Wilson and Head, 1983). Given the low eruption velocity at the vent and the narrow range of conditions needed to sustain plumes on Venus, column collapse resulting in PDCs is likely to be the primary means of depositing pyroclastic material with long runout distances on the surface (Head and Wilson, 1982; Sugita and Matsui, 1993; Thornhill, 1993). Fagents and Wilson (1995) proposed an alternate mechanism for pyroclast dispersal by intermittent Vulcanian activity. However, their study predicts localized blocky ejecta deposits extending < 1 km from the source. While this mechanism of pyroclast emplacement is possible on Venus, it does not address the long runout pyroclastic deposits. To date, there have not been any detailed studies of the actual processes and controls involved in emplacing long runout

pyroclastic deposits on Venus. In the study presented here, we investigate the formation of long runout pyroclastic deposits on Venus using pyroclastic flow models adapted to Venus's ambient conditions. Bearing in mind that exceptionally high volatile contents are needed to achieve explosive activity on Venus, we focus our efforts primarily on understanding the lower limit of explosive eruption conditions (such as minimum column height, minimum eruption duration, etc.) needed for the emplacement of long runout deposits on Venus's surface.

PDC modeling generally involves characterizing a PDC as either a gravity-driven, high particle concentration flow (Kelfoun and Druitt, 2005; Sheridan *et al.*, 2005), herein referred to as a pyroclastic flow; or a dilute surge driven by turbulence and density contrast (Bursik and Woods, 1996; Dade and Huppert, 1996), herein referred to as a dilute current. The dense PDC models also find application in modeling other types of gravity-driven granular flows that show very little mixing with the ambient fluid, like subaerial and submarine debris flows, and submarine slides (White, 2000; Denlinger and Iverson, 2001, 2004; Pitman and Long, 2005; George and Iverson, 2014). The dilute PDC models are ideal for modeling turbulent, low particle concentration currents that are controlled by mixing at the flow front (Dade and Huppert, 1995b, 1995a). Flows of this kind also include turbidity currents that emplace long runout turbidites under water. On Venus, the theorized eruption of denser pyroclast at lower velocities (Head and Wilson, 1986) lends support for transport by pyroclastic flows (capable of supporting larger, denser particles) rather than dilute currents (more suited to transporting fines). The high radar backscatter and CPR values of the deposits are thought to arise from centimeter-sized clasts transported over several tens of kilometers (Campbell *et al.*, 2017), also indicating possible transport by dense pyroclastic flows. The scope of the modeling work presented here is hence limited to the simulation of dense pyroclastic flow transport on Venus. We use a 2D gravity-driven mass flow model with two different initiation mechanisms to simulate pyroclastic flows fed from (1) a collapsing column and (2) a sustained fountain. The modeled deposit extents are then systematically compared with the SAR data to constrain some of the physical properties of the pyroclastic eruptions that could have emplaced the observed deposits.

In section 2, we briefly describe the proposed pyroclastic deposits of interest and the datasets used for mapping them. The 2D flow model, along with underlying assumptions, limitations and assessment techniques are discussed in section 3. The model results are discussed and evaluated against observed deposit extents in section 4. We end with a discussion of pyroclastic flow

dynamics on Venus and attempt to place possible pyroclastic volcanism on Venus within the context of known terrestrial eruptions in section 5.

2 Proposed pyroclastic deposits on Venus

Magellan left-look SAR images (~100 m spatial resolution) and stereo-derived topography maps (~1-2 km spatial resolution) created from Magellan left-look SAR images (Herrick *et al.*, 2012) were used for mapping the proposed pyroclastic deposits. The two regions with proposed pyroclastic deposits that fall within the covered extent of both the backscatter and the stereo-derived topography datasets are (1) Irnini Mons and Anala Mons in Western Eistla and (2) Pavlova Corona and Didilia Corona in Eastern Eistla (Figure 1).

2.1 Western Eistla Regio

Irnini Mons (14.3°N, 15.65°E) is a volcano-tectonic construct at an elevation of ~1.75 km above the MPR with coronae-like features at its summit (McGill, 1998). At the center of Irnini Mons is the 225-km diameter Sappho Patera, classified as a concentric corona (Stofan, 1992). Two radar-bright deposits, marked I1 and I2 in Figure 1, appear to originate along the fractures bounding Sappho Patera to the north and extend down slopes of ~1.5° up to distances of 70 - 100 km. Numerous grabens can be seen extending along the length of deposit I1, specifically to the south. Lava flows with high backscatter (possibly caused by high surface roughness) appear to emerge from under unit I1 to the northwest (Campbell *et al.*, 2017). Unit I2 to the northeast of Sappho Patera appears to cross the concentric ridges and extend down into the summit depression. Another proposed pyroclastic deposit in the region is unit I3 to the west of Irnini Mons (Figure 1a). I3 is situated in a topographic low and has been suggested to be an erosional remnant of a much larger I1 deposit (Campbell *et al.*, 2017).

To the southwest of Irnini Mons and with similar coronae-like features is the volcanic center of Anala Mons (McGill, 1998) at an elevation of ~2.25 m above the MPR. Anala Mons's summit is smaller and more complex than the simple circular depression at Irnini Mons. A diffuse-margined high-radar backscatter deposit, marked A1 in Figure 1, can be seen covering the northern and northwestern flanks of Anala Mons. Similar to I1 and I2, the volcanic flank on which deposit A1 has been emplaced has a low average slope of ~1°.

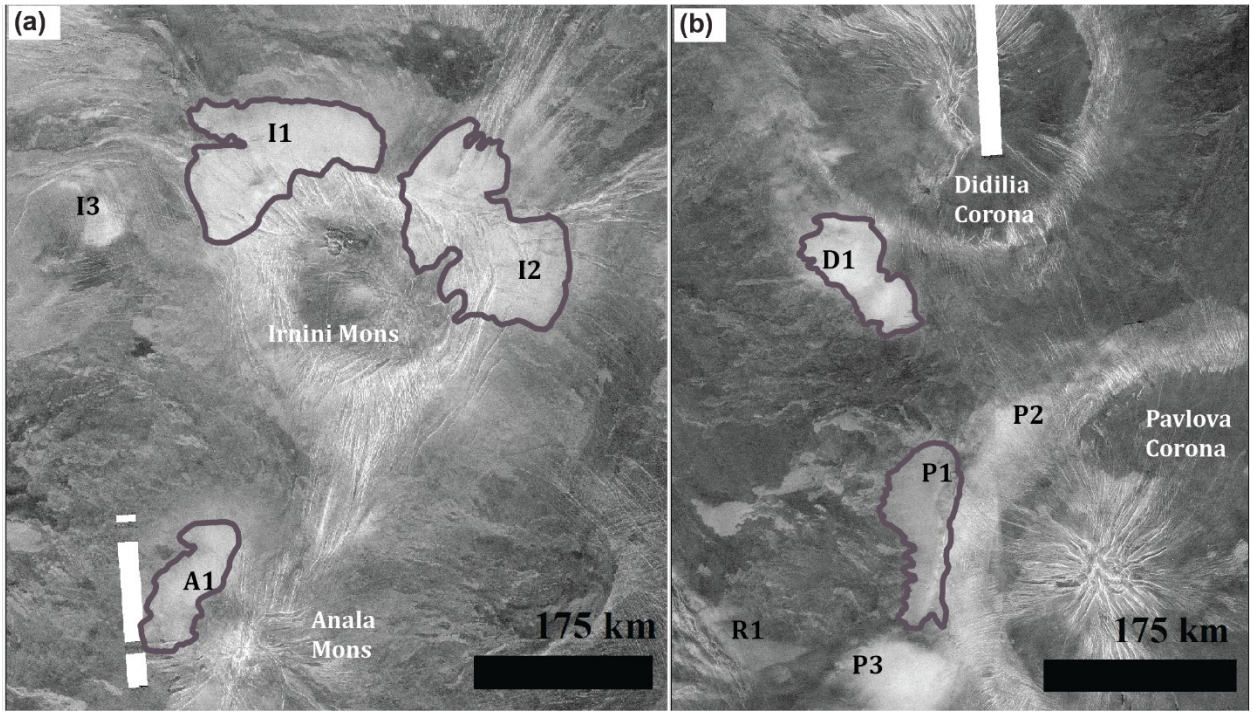

Figure 1. Magellan left-look SAR image of (a) Western Eistla Regio showing Irnini Mons and Anala Mons and (b) Eastern Eistla Regio showing Didilia Corona and Pavlova Corona. The radar bright, proposed pyroclastic units modeled in this study have been labeled and marked in thick outlines. Nearby radar-bright units, also proposed to be pyroclastic material but not investigated in this study, have been labelled.

2.2 Eastern Eistla Regio

Units with diffuse margins near the western flank of Pavlova Corona (14.5°N, 40°E) and on the southwestern flank of Didilia Corona (18°N, 37.3°E) have also been mapped as coarse textured pyroclastic deposits (units P1, P2, P3, D1 and R1 in Figure 1b) (Campbell and Clark, 2006). Both coronae have densely lineated material at the center surrounded by volcanic plains material within the summit. The proposed pyroclastic deposits extend downwards along slopes of ~1.5° from the coronae rims which are also made of densely lineated material.

While Magellan SAR and altimetry datasets are available for all the units discussed above, the higher resolution stereo-derived topography only covers deposits I1, I2, I3, A1, P1 and D1. We model pyroclastic flows at all these locations except I3 which is not a summit deposit and has no clear flow direction.

3 Modeling dense pyroclastic flows

3.1 Numerical model

The pyroclastic flow is modeled as a two-component mixture of solids suspended in a Newtonian fluid. A 2D depth-averaged model, which assumes that flow properties in the horizontal direction are independent of its height, is solved with suitable source terms to determine the flow thickness and velocity at each point on a 2D topographic grid as a function of time t. The mass (equation (1)) and momentum conservation equations (equations (2) and (3)) of the model are given below.

$$\frac{\partial h}{\partial t}+\frac{\partial (hu)}{\partial x}+\frac{\partial (hv)}{\partial y}=K \tag{1}$$

$$\frac{\partial (hu)}{\partial t}+\frac{\partial}{\partial x}\left(hu^2+\frac{1}{2}g_z h^2\right)+\frac{\partial (huv)}{\partial y}=g_x h-sgn(u)(1-\lambda)g_z h\mu-\frac{2uv_f\mu}{\rho h} \tag{2}$$

$$\frac{\partial (hv)}{\partial t}+\frac{\partial (huv)}{\partial x}+\frac{\partial}{\partial y}\left(hv^2+\frac{1}{2}g_z h^2\right)=g_y h-sgn(v)(1-\lambda)g_z h\mu-\frac{2vv_f\mu}{\rho h} \tag{3}$$

Here, K is a source term used for implementation of different initiation styles (discussed more in section 3.3), h is the flow thickness, u is the depth-averaged velocity in the x-direction and v is the depth-averaged velocity in the y-direction, g_z is the acceleration due to gravity acting perpendicular to the surface, λ is the ratio of excess pore fluid pressure to total normal stress at the base of the flow, μ is the shear rate dependent basal friction coefficient, v_f is the volume fraction of fluid in the flow, μ is the viscosity of the interstitial fluid, and ρ is the bulk density of the flow. The mass and momentum conservation equations can also be written in vector form as

$$U_t+F(U)_x+G(U)_y=S_x+S_y \tag{4}$$

where $U=\begin{bmatrix} h \\ hu \\ hv \end{bmatrix}$ (5)

represents the conserved quantities, and

$$F(U)=\begin{bmatrix} hu \\ hu^2+\frac{1}{2}g_z h^2 \\ huv \end{bmatrix} \tag{6}$$

$$G(U)=\begin{bmatrix} hv \\ huv \\ hv^2+\frac{1}{2}g_z h^2 \end{bmatrix} \tag{7}$$

are the fluxes in x and y directions, respectively. S_x and S_y are the source terms comprising eruption rate (indicated by the terms on the right-hand side of equation (1)), and gravitational forcing, basal frictional resistance, and viscous stresses in the x and y directions, respectively (indicated by the terms in the same order on the right-hand side of equations (2) and (3)). We use a 1st order Godunov scheme with an HLLC Riemann solver to calculate the flux $F(U)$ in the x direction and flux $G(U)$ in the y direction across cell interfaces on the 2D grid (Toro *et al.*, 2001; Toro, 2009). The source terms S_x and S_y are solved separately using an explicit Euler method.

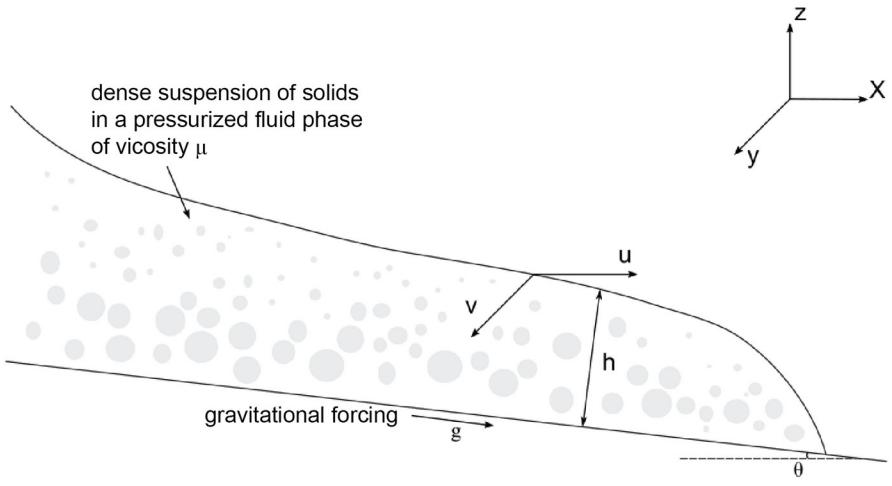

Figure 2. Schematic of the dense pyroclastic flow model along one of the horizontal directions (x-direction). The pyroclastic flow propagates as a mixture of solids (ash and lithics) supported in a pressurized fluid phase. Quantities h, u and v are the flow thickness, and depth averaged velocity in x-direction and velocity in y-direction, respectively. The flow is driven by gravity $g = 8.87\, m\, s^{-2}$ on Venus and topographic slope θ. Resistance to the flow is provided by interparticle and basal friction, and viscous stresses within the fluid.

We use Magellan stereo-SAR digital elevation models (DEMs) (Herrick *et al.*, 2012) resampled to 200 m/pix spatial resolution to compute the topographic slope in the x and y directions. It should be acknowledged that the post-depositional topography is naturally bound to be different from the topography on which the pyroclastic deposits were emplaced. In addition, many coronae formation models invoke topographic uplift followed by relaxation, indicating possibly steeper paleotopography before emplacement of the deposits (Stofan, 1992; Smrekar and Stofan, 1997; Dombard *et al.*, 2007). Determining the pre-flow topography would require knowledge of the thickness of the deposit, age of the deposit, and amount of possible lithospheric relaxation, which cannot be determined with currently available datasets. Hence, our model is limited by the assumption that the current topography is representative of the pre-flow topographic trend.

The x and y coordinates of the model grid are tied to the coordinates of the input topography dataset. Therefore, the accuracy and resolution of the topography data largely determines how well elevations and slopes are represented in the model. Even though the 1-2 km spatial resolution of the stereo-derived DEM is better than the 10-20 km resolution of Magellan altimetry-derived DEM, the resolution is still not fine enough to capture high frequency variations in topography. While the general background slope is well-represented, smaller topographic variations such as narrow channels, small domes, cones, pits, or craters would not be resolvable. Hence, some of the known pyroclastic flow behaviors such as channelization, local pooling of deposits in topographic lows, and overriding of deposits on local slopes cannot be modeled due to data resolution limitations. Additionally, locations where there are data gaps from the stereo-processing of SAR images have been filled in with values from the coarser resolution Magellan altimetry data. This results in artificial steps in topography along the boundary between the two datasets; the effects of this are discussed briefly in section 5.1.

The flow motion is opposed by viscous stresses in the interstitial fluid and friction at the base of the flow. We use a shear-rate dependent variable basal friction model to determine the frictional resistance as the flow evolves (Jop *et al.*, 2006). The basal friction coefficient is given by,

$$\mu(I)=\mu_s+\frac{(\mu_2-\mu_s)}{\frac{I_0}{I}+1} \quad (8)$$

where the critical friction coefficient $\mu_s=\tan(20.9°)$, the limiting friction coefficient $\mu_2=\tan(32.76°)$ and the constant $I_0=0.279$ are empirical parameters. The inertial number I is given by,

$$I=\frac{\dot{\gamma}\,d}{\sqrt{\frac{P}{\rho_s}}} \quad (9)$$

where $\dot{\gamma}$ is the shear rate computed as $2\sqrt{u^2+v^2}/h$, d is the mean particle diameter, P is the basal normal stress, $\rho_s$and is the density of the solid in the mixture. The calculated coefficient of friction $\mu(I)$ varies from μ_s at zero velocity to a limiting value of μ_2 at higher velocities.

The flow is assumed to be composed of 30% solids by volume ($v_f=0.7$ in the model), supported by excess interstitial pore fluid pressure. The excess pore fluid pressure is thought to be important in enabling propagation of pyroclastic flows for several tens of kilometers on sub-horizontal slopes lower than the typical angle of rest for granular flows (Druitt, 1998; Druitt *et al.*, 2004, 2007; Roche, 2012). In some cases, pore fluid pressure values equivalent to the total stress at the bed (completely fluidized flow) can develop (Dufek, 2016). High pore fluid pressure is accounted for in the model by using initial values of $0.90>\lambda>0.99$ in order to simulate highly fluidized flows. Degassing of pyroclastic flows during transport and subsequent decay of pore fluid pressure is also accounted for in the model by incorporating pore pressure diffusion (Montserrat *et al.*, 2012; Roche, 2012); this is achieved using equation (63) in Iverson and Denlinger (2001), assuming a constant diffusivity of $0.01\,m^2\,s^{-1}$.

We use constant values for fluid density $\rho_f=65\,kg\,m^{-3}$ (atmospheric density at the surface of Venus) and solid density $\rho_s=2600\,kg\,m^{-3}$ (consistent with basaltic magma densities used in Head and Wilson (1986), Airey *et al.* (2015)) yielding a constant bulk density of $\rho\ \ 825\,kg\,m^{-3}$ for the

mixture. Unlike turbulent suspensions, for which entrainment of ambient air is a significant factor affecting runout, slow-moving (< ~100ms^{-1}) granular flows are not energetic enough to entrain large amounts of ambient fluid (Druitt, 1998). Ambient air entrainment, even if occurring, will likely not lead to significant gas expansion in the flow owing to the high temperature of the entrained air (~737 K at Venus's surface) (Head and Wilson, 1986). Using a constant bulk density is therefore appropriate in our case where we expect negligible atmospheric mixing and flow expansion. We use an effective fluid viscosity of $\mu = 10^{-4}$ Pas for all model simulations, consistent with the viscosity of CO_2 at 737 K. This is slightly higher than the typical viscosity of $\mu = 10^{-5}$ Pas used in terrestrial pyroclastic flow models (Wilson and Head, 1981; Roche, 2012). It should be noted viscous stresses are thought to be less significant for flows with large thicknesses (Denlinger and Iverson, 2001), hence the final flow properties are expected to be less sensitive to the choice of viscosity.

The total simulation duration varies from deposit to deposit depending on the amount of time required for the flowing mass to come to a stop. Flow velocity ¿$0.01\,m\,s^{-1}$ was used as the stopping criterion to determine when the flow comes to rest. Pyroclastic flow deposits are thought to form either *en masse* (formation of a deposit as a whole when the entire flow comes to rest) (Sparks et al., 1973; Sparks, 1976) or by progressive aggradation (incremental, sustained deposition from the base of a density-stratified current) (Fisher, 1966; Branney and Kokelaar, 1992). *En masse* deposition involves a flow with a laminar, deflated, plug-like interior that slides on a basal fluidized layer. Progressive aggradation would occur from a vertically stratified current having different particle concentrations and velocities for each layer. Since we use a depth-averaged scheme which does not capture variations in model variables in the z-direction, the deposition mechanism modeled here, by default, is *en masse* deposition. This is a suitable approach in view of experiments showing that high particle-concentration flows (27.5% - 40% volume of solids, similar to the flows considered here) come to an abrupt halt resulting in thick deposits (Hallworth and Huppert, 1998).

3.2 Assessment of the model performance

In order to quantitatively assess if the observed deposits could have been emplaced by the types of pyroclastic flows modeled here, we need an objective approach for comparing the results from our 2D simulations to variables that can be measured from Magellan data. For terrestrial mass

flow models, the compared variables of interest typically include runout distance, thickness, and spatial extent of the deposit. Since we do not have precise measurements of the deposit thickness and the vent location from Magellan observations, we only compare the simulated area of deposition $\widehat{A}$ with the reference area A mapped from Magellan SAR data using the approach developed in Heiser *et al.* (2017). The variable A accounts for deposit location and shape in addition to the 'magnitude' of deposit area. We compute a similarity index given by $\Omega = \alpha - \beta - \gamma$ to evaluate the fit between $\widehat{A}$ and A for each modeled deposit. Here, α is the overlap between the reference and simulated area (aka true positive), β represents underestimation (aka false negative) where the model has not predicted any emplacement at locations where deposits are present in the data and γ represents overestimation (aka false positive) where the model has predicted deposition outside the bounds of the deposit mapped from data. To compute these quantities, the final 2D thickness maps for all simulated deposits are converted into binary rasters with a threshold deposit thickness of $h = 20\,cm$. The binary rasters from the model results were then evaluated on a pixel-by-pixel basis at 200 m/pix resolution against the boundaries of the mapped deposits to determine α(the number of 'true positive' pixels), β(the number of 'false negative' pixels), and γ(the number of 'false positive' pixels). The possible range of Ω values vary from -1 to 1 with $\Omega = 1$ representing a complete overlap between the simulated and mapped deposit. For each deposit, we compute Ω values corresponding to all combinations of parameters listed in Table 1. The combination of parameters that result in the highest Ω value for each deposit is considered the best-fit set of model parameters for the deposit.

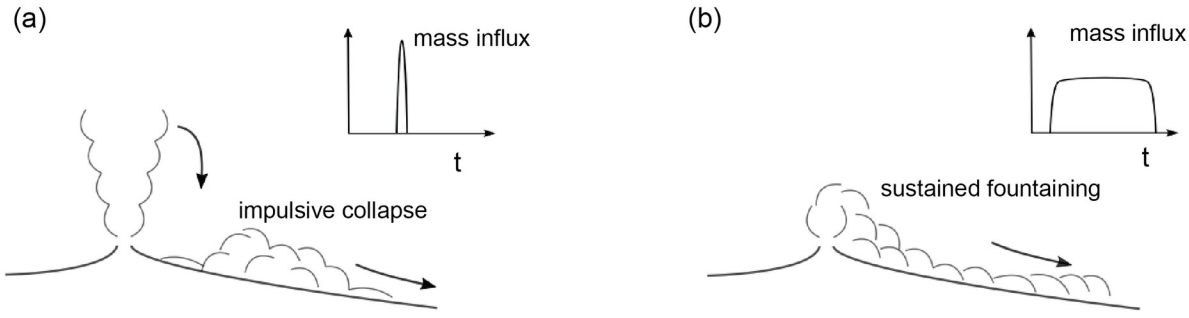

Figure 3. Schematics of the two PDC initiation mechanisms modeled (modified from Branney and Kokelaar (2002)). (a) Short duration PDC generated by a discrete column collapse; (b) Prolonged low fountaining resulting in a steady flow.

3.3 Initial conditions

3.3.1 Vent location and geometry

The exact location and the geometry of the vents that sourced the proposed pyroclastic deposits near the volcanic and coronal summits cannot be identified at the available dataset resolution (Grosfils *et al.*, 2011; Campbell *et al.*, 2017). The large extent of the mapped deposits would likely require emplacement by voluminous flows from several eruptions distributed in space and time. In addition, early test runs of the model suggested that lateral spreading of the modeled flow is fairly minor; hence, multiple vents were needed to reproduce the observed deposits. However, the possibility of multiple episodes of explosive activity in the same volcanic zone on Venus is not very clear. Many ignimbrite deposits on Earth are known to have formed from multiple fissures or vents associated with a caldera, in the case of both felsic (Hildreth and Mahood, 1986; Self *et al.*, 1986; Holohan *et al.*, 2008; Wilson, 2008; Jessop *et al.*, 2016) and intermediate to basaltic eruptions (Robin *et al.*, 1994; Allen, 2004; Burgisser, 2005; Giordano *et al.*, 2006; Rooyakkers *et al.*, 2020). The source vents along the caldera margins can also migrate over time feeding multiple PDCs (Holohan et al., 2008). Similarly, multiple eruptions from fissures along the summit ring fractures could have occurred on Venus given that Irnini Mons, Didilia Corona and Pavlova Corona have a summit subsidence feature. For the purpose of this study, we proceed to model PDCs originating from different linear vents located in the ring fracture systems at the summit. The choice of linear vent geometry was made taking into consideration studies that have shown that linear vents favor column collapse and ignimbrite generation compared to circular vents (Glaze *et al.*, 2011; Jessop *et al.*, 2016). Continuous strings of pixels, representing linear vents, at locations of highest elevation in the annular fractured terrain were fixed as the source cells for the flow. Observations of historic basaltic fissure eruptions indicate that active linear vents are generally limited to lengths of no more than a few kilometers (e.g., Walker, 1984; Thordarson and Self, 1993). In this model we use vents that are 5 km long (the maximum vent length used by Glaze *et al.* (2011)) and 0.2 – 1.2 km wide. Exploring different vent widths allowed us to simulate a range of flow volumes without having

to use exceptionally large column heights. The vents are assumed to be spaced apart from one another at a constant distance of ~5 km. The total number of vents used for each deposit was determined based on the lateral extent of the deposit. The geometry of the resulting volcanic columns in this scenario would be complex 'curtains' (similar to the eruptions columns theorized by Hildreth and Mahood (1986)) rather than cylindrical structures.

3.3.2 Mechanisms of initiation

Large, voluminous PDCs can result either from impulsive collapse of large volcanic columns or through long-lived, low fountaining eruptions (Figure 3). We model PDCs generated by both styles of initiation by modifying the source term in the mass conservation equation (equation (1)) in our model. The column collapse initiation mechanism is modeled by allowing the total flow volume to collapse at time t=0 i.e., the entire mass of the column that goes into feeding the PDC is introduced into the simulation at time t=0. The source term K in equation (1) is set to 0 for this initiation style. For modeling fountain-fed flows, all the vent cells are assumed to feed a steady current for a fixed fountaining duration (i.e., for time $t \leq t_{fountain}$). The total volume of material to be simulated is distributed evenly across the feeding cells i.e., each cell is assumed to have the same eruption rate (expressed in ms^{-1}). This is implemented by setting the source term K in equation (1) equal to a constant eruption rate (expressed as the change in thickness *h* with time) for the duration of fountaining (see equation (10)). The source term is reset to 0 after the end of fountaining. This constant influx rate approach does not capture waxing and waning eruption rates. We use this simplification since the change in eruption rates over the course of an eruption cannot be determined without either observations made during the eruption or field measurements of the deposit.

$$\frac{\partial h}{\partial t}+\frac{\partial (hu)}{\partial x}+\frac{\partial (hv)}{\partial y}=K=\begin{cases} h_{fountain}, \wedge t \leq t_{fountain} \\ 0, \wedge t > t_{fountain} \end{cases} \quad (10)$$

For both styles of pyroclastic flow generation, the initial volume of material has dimensions with the thickness nearly equal to or even greater than the length scales in the XY plane. Especially in the case of impulsive collapse, the collapse height to vent width ratio ranges from 2 to 7 for deposits A1, D1 and P1 and is as high as 10 for the larger I1 and I2 deposits. This results in high initial velocities and likely turbulent transport when the flow initiates. Such flow dynamics are not captured effectively by the depth-averaged approach used here, which relies on very little to

no mass or momentum transfer in the z-direction in comparison to the flow's areal extent. However, soon after initiation, the flow evolves away from large initial flow depths and velocities (see section 5.2 and Figure 7e) making this model well suited for describing the flow during most of its transport duration.

Assessing the sensitivity of the model to changes in the initial conditions associated with both styles of initiation will help narrow down the source conditions likely to give rise to the observed deposit properties. By stepping through a range of column heights (for impulsive collapse initiation), fountaining rate and fountaining duration (for sustained fountaining initiation), and initial pore fluid pressure (for both styles), we approximate source conditions associated with more or less energetic versions of these two eruption styles. The initial conditions explored for both styles of initiation are given in Table 1. Using higher eruption rates and collapse heights than those explored in our models, while likely to result in slightly higher values of overlap between the simulated area of deposition and the reference area, would also result in higher flow velocities eventually leading to turbulent flow regimes which cannot be suitably described by our model. In addition to the values listed in Table 1, the initial pore fluid pressure was also varied; the values used were $\lambda = 0.90, 0.95, 0.98, 0.99$. A total of 144 simulations for collapse-fed initiation and 80 simulations for fountaining style initiation were performed. Each model simulation was evaluated using the approach described in section 3.2; the input parameters to the model that resulted in the highest similarity index for each deposit (Table 2) was considered to be the most likely source conditions associated with that pyroclastic deposit. For all further discussions of trends in the results that were found to be common to all the modeled deposits, we use deposit P1 as a representative example.

Impulsive collapse initiation		
Deposit	Vent width (km)	Collapse height (km)
A1, P1, D1	0.2, 0.4, 0.6, 0.8, 1.0, 1.2	0.4, 0.6, 0.8, 1.0, 1.2, 1.4
I1, I2	0.2, 0.4, 0.6, 0.8, 1.0, 1.2	0.4, 0.6, 0.8, 1.0, 1.2, 1.4
Sustained fountain-fed initiation		
Deposit	Fountaining duration (s)	Eruption rate $(m\,s^{-1})$
A1, P1, D1	200, 300, 400, 500	5, 15, 25, 35, 50
I1, I2	300, 400, 500, 600	5, 15, 25, 35, 50

Table 1. Values for parameters used in modeling flows from discrete collapse and sustained fountaining. A similar range of the parameter space was explored for all deposits. The parameter values for deposits I1 and I2, which are larger in area than P1, D1 and A1, are higher.

Impulsive collapse initiation					
Deposit	Column height (km)	Initial ratio of pore fluid pressure to basal normal stress (λ)	Total volume (km^3)	Mean thickness (m)	Similarity index Ω
P1	1200	0.99	167	20 ± 11.8	0.158
D1	1400	0.99	173	23.6 ± 12	0.028
A1	1400	0.95	141	23.3 ± 15.4	0.319
I1	2000	0.99	331	22.4 ± 13.9	0.096
I2	2000	0.99	313	20.2 ± 18.5	0.234

Sustained fountain-fed initiation						
Deposit	Eruption rate (ms^{-1})	Fountain duration (s)	Initial ratio of pore fluid pressure to basal normal stress (λ)	Total volume (km^3)	Mean thickness (m)	Similarity index Ω
P1	50	400	0.99	232	55 ± 35	0.232
D1	50	500	0.99	461	65 ± 30.5	0.131
A1	50	400	0.99	282	47.2 ± 26.2	0.258
I1	50	600	0.99	724	61.8 ± 32.5	0.069
I2	50	700	0.99	784	71.2 ± 65	-0.102

Table 2. Table showing the combination of input parameters and resulting variables corresponding to the highest value of similarity index Ω for each deposit.

4 Results

4.1 Impulsive column collapse

Final flow extent maps for impulsive collapse-fed flows corresponding to model parameters that resulted in the highest similarity index between the mapped and the modeled deposits are shown in Figure 4. Figures 4a to 4e show the mapped outline of the proposed pyroclastic deposits and

Figures 4f to 4j show the extent of the deposits modeled from a collapse-fed flow. There is only 51%- 65% overlap between the extents of the observed and the modeled deposits, pointing to the exceptionally large area of the proposed pyroclastic deposits. There is no significant difference in the percentage overlap between the smaller (P1, D1 and A1) and the larger (I1 and I2) deposits, or in the percentage overlap between the deposits of Western Eistla Regio (I1, I2 and A1) and Eastern Eistla Regio (P1 and D1).

Flow velocity, thickness, and runout distance of impulsive collapse-fed flows are primarily governed by changes to the height of collapse (flow velocity $v \propto \sqrt{2gH_0}$ where H_0 is the collapse height). Taller columns generate faster flows capable of achieving longer runouts. This is evident in Figure 5a, which shows the runout distances for deposit P1 for flows of comparable volumes ($85 \pm 2\,km^3$) produced by columns collapsing from three different heights – $0.6, 0.8$and $1.0\,km$. The runout distances were measured along the transect A-A' (shown in Figure 4a). Though we have no measurements of the actual deposit thickness, it is still interesting to look at the modeled thickness, as radar observations suggest that the deposits maybe less than a few tens of centimeters thick at the margins (Campbell *et al.*, 2017). Gradual thinning of the deposits away from the source is seen for all cases of collapse height, however the thickness at the terminus of the deposit is still >10 m (Figure 5a). Proximal to the source (< 10 km from the source), there is no noticeable difference in the final thickness between the different flows. Differences in final flow thicknesses, resulting from minor differences in volume, are observable only near the terminus.

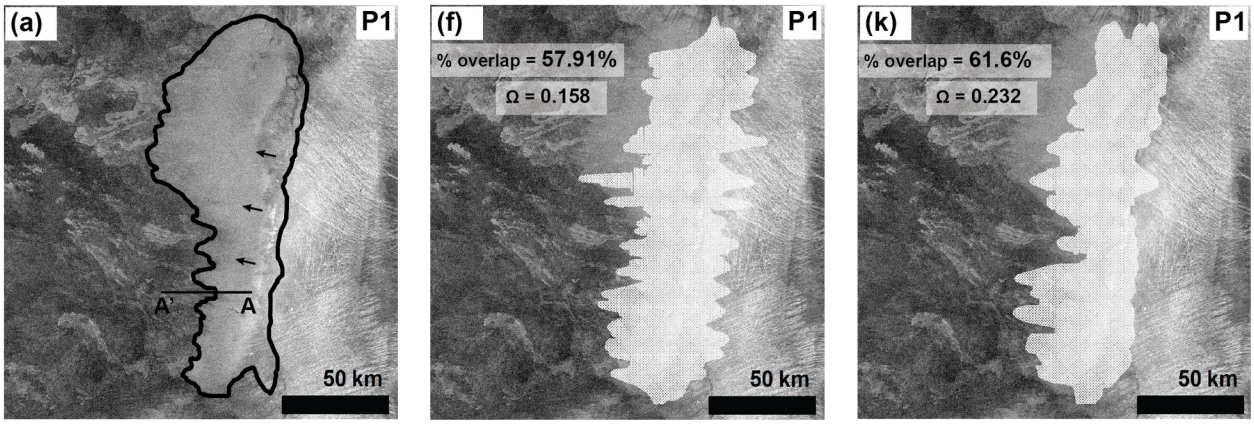

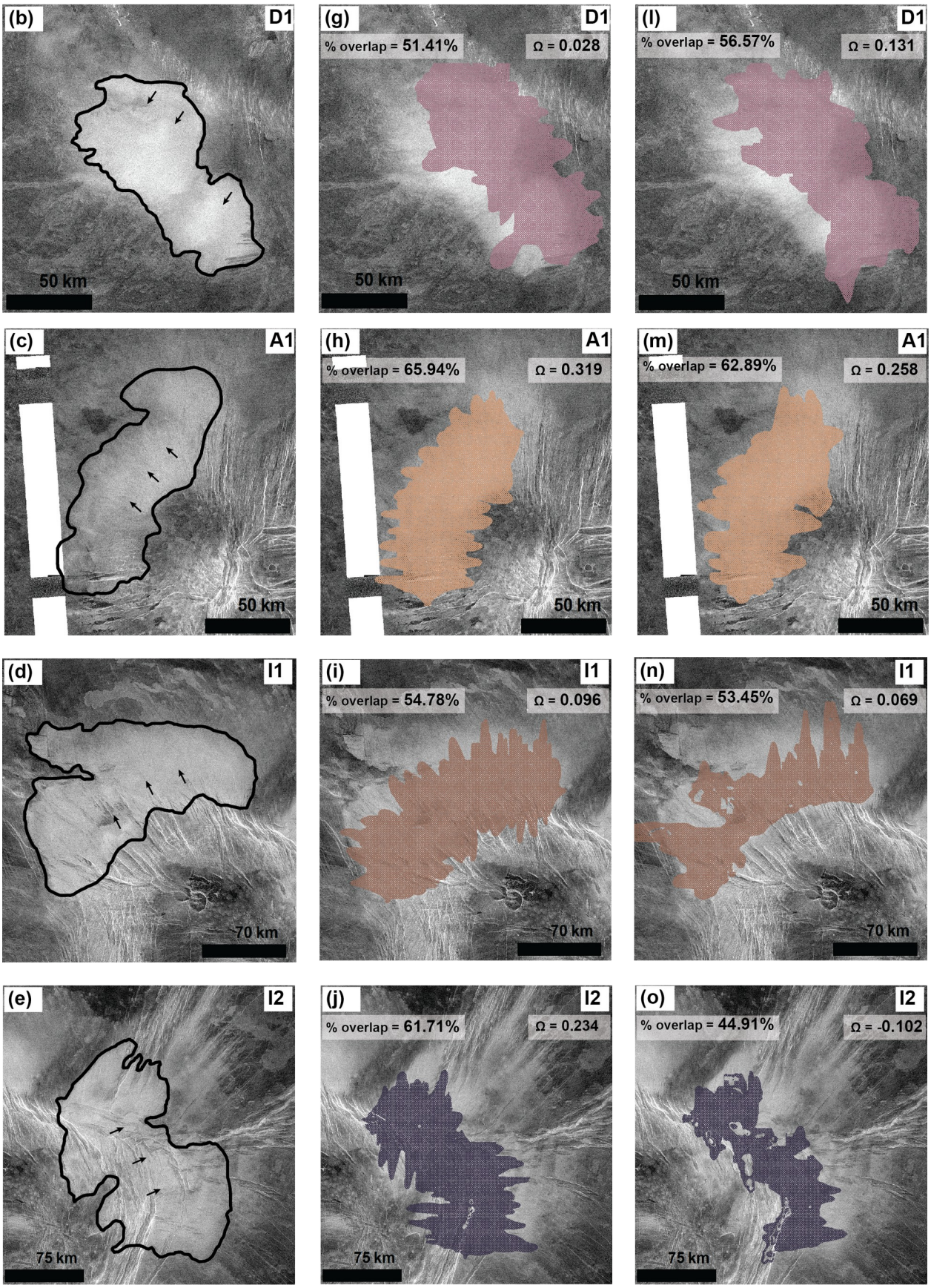
(b)
D1
50 km
(g)
D1
% overlap = 51.41%
Ω = 0.028
50 km
(l)
D1
% overlap = 56.57%
Ω = 0.131
50 km
(c)
A1
50 km
(h)
A1
% overlap = 65.94%
Ω = 0.319
50 km
(m)
A1
% overlap = 62.89%
Ω = 0.258
50 km
(d)
I1
70 km
(i)
I1
% overlap = 54.78%
Ω = 0.096
70 km
(n)
I1
% overlap = 53.45%
Ω = 0.069
70 km
(e)
I2
75 km
(j)
I2
% overlap = 61.71%
Ω = 0.234
75 km
(o)
I2
% overlap = 44.91%
Ω = -0.102
75 km

Figure 4. (a)-(e) Magellan SAR images with the proposed pyroclastic deposits P1, D1, A1, I1 and I2 outlined in black. The black line marked A-A' is the transect along which flow thicknesses are compared and studied. (f)-(j) Magellan SAR images showing the extent of the deposits (P1, D1, A1, I1, I2) modeled from column collapse using parameters listed in table 3. (k)-(o) Magellan SAR images showing the extent of the deposits (P1, D1, A1, I1, I2) modeled from sustained fountaining using parameters listed in table 3. The percentage area of overlap between the mapped deposits shown in (a)-(e) and the model results (f)-(o), and the similarity index Ω are mentioned at the top of the modeled deposit panels. Inferred flow direction are indicated by black arrows in panels (a)-(e). The modeled flow travels predominantly along the inferred flow direction with limited spreading in the upslope direction for all deposits.

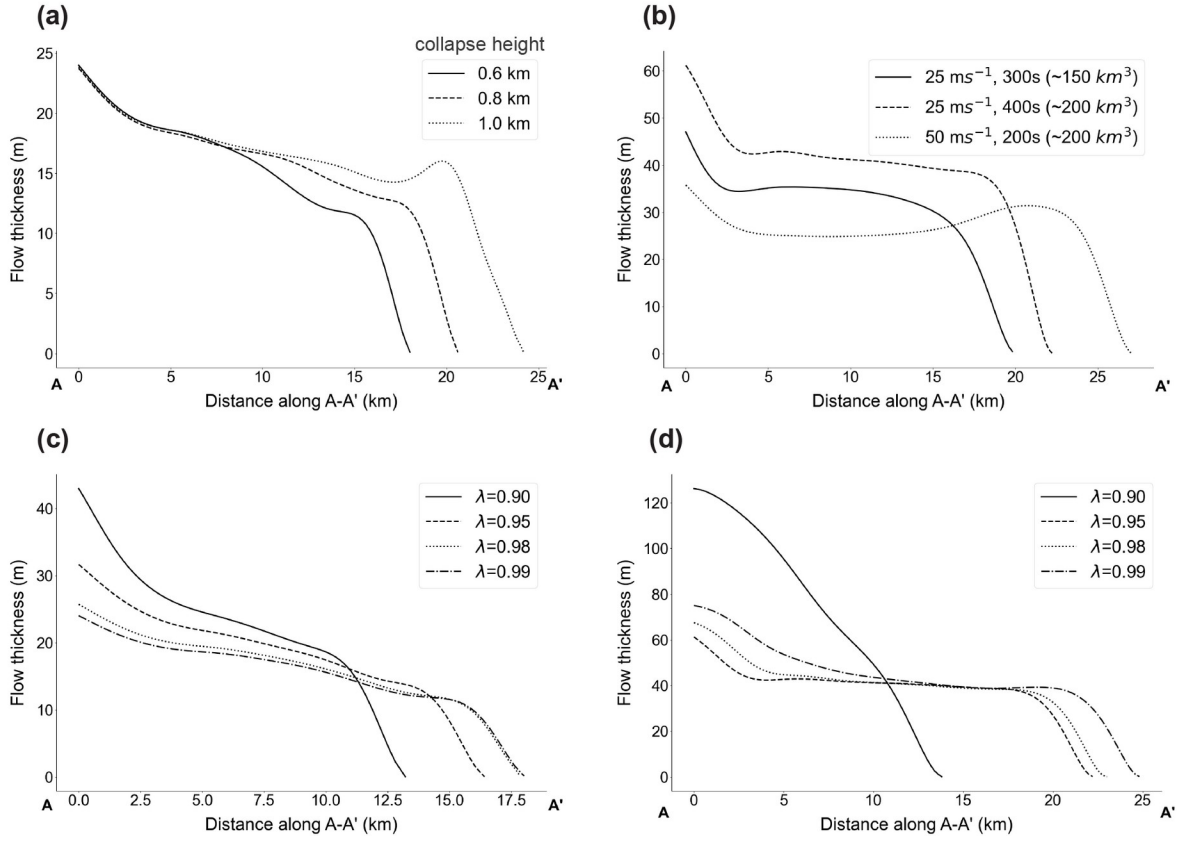

Figure 5. (a) Flow thickness of collapse-fed flows is shown as a function of distance along A-A' for different collapse heights H_0 = 0.6, 08, 1.0 km. Collapse of taller columns result in longer runout. (b) Flow thickness of fountain-fed flows is shown as a function of distance from the source along A-A' for different eruption rates and duration. The dashed and dotted curves represent flows of volume $200\,km^3$. fed by eruptions of different durations. The solid curve

463 shows the profile along a smaller flow of volume $150\,km^3$ For similar volumes, flows that are
464 erupted at a higher rate achieve for longer runout distances. (c) Flow thickness as a function of
465 distance along A-A' for different initial pore pressure conditions λ=0.9, 0.95, 0.98, 0.99 for
466 collapse-fed flows. (d) Flow thickness as a function of distance along A-A' for different initial
467 pore pressure conditions λ=0.9, 0.95, 0.98, 0.99 for fountain-fed flows.

468 4.2 Sustained pyroclastic fountaining

469 Figures 4k to 4o show the final flow extent maps from fountaining simulations corresponding to
470 model parameters that resulted in the highest similarity index between the mapped and the
471 modeled deposits. The percentage of simulated deposit area that matches the observed extent
472 varies from 45%-63%. This range is slightly lower than the range of overlap percentages
473 obtained for collapse-fed flows. With regard to individual deposits, fountaining initiation results
474 in higher Ω values than collapse initiation for the Eastern Eistla Regio deposits, and lower Ω
475 values for the Western Eistla Regio deposits. In particular, the fountain simulations do a poor job
476 of reproducing the deposit extent of the large deposits I1 and I2 at Irnini Mons (Figures 4n and
477 4o).
478 We investigated the sensitivity of the fountain-fed flows to changes in fountaining height
479 (expressed as eruption rate in $m\,s^{-1}$) and duration. An increase in either of these parameters leads
480 to more voluminous pyroclastic flows capable of emplacing pyroclastic material over a more
481 extensive area. We find that the flow runout is more sensitive to changes in mean eruption rate
482 when compared to the fountaining duration. For the same vent area, an increase or decrease in
483 the eruption rate would manifest as a change in the fountain height. Higher fountains impart
484 more kinetic energy to the flow causing the pyroclastic flow to runout farther. This is clearly
485 seen in the simulations for deposit P1, where a pyroclastic flow with a volume of $200\,km^3$
486 resulting from a 200s long fountaining episode with a higher mean eruption rate (50 ms^{-1}) (dotted
487 curve in Figure 5b) has ~1.25 times the runout compared to a flow of same volume resulting
488 from a longer eruption (400 s) at half the mean eruption rate (dashed curve in Figure 5b).
489 Fountaining duration plays a relatively less important role in our models in promoting runout,
490 when compared to the fountain height. For instance, a smaller, short-duration pyroclastic flow
491 fed by $150\,km^3$ of material erupted at the same rate as a longer-lived $200\,km^3$ volume flow has
492 almost similar runout to the longer duration flow (solid and dashed curves in Figure 5b). The

493 simulations show that longer eruption durations primarily lead to spatially uniform thickening of
494 the deposit. Even though longer eruptions lead to extrusion of more volume available for the
495 flow, our simulations show a deposit 'pile-up' effect at relatively short distances from the source
496 caused by the rapid deceleration, unless the initial flow velocity is high. Unlike results from the
497 collapse-fed flow simulations that show gradual thinning of the deposit away from the source,
498 final deposit thickness obtained from fountain-fed flows appears to be nearly uniform in many
499 places, except very close to the source and at the margins.

500 4.3 Effect of fluidization

501 Our models indicate that fluidization is a critical factor in determining the final runout distance
502 of the pyroclastic deposits investigated. High excess pore fluid pressure can promote longer
503 runouts by effectively reducing interparticle friction (Sparks, 1978; Wilson, 1984; Druitt *et al.*,
504 2004). Especially in gently sloping areas like our study sites, where there is no steep topography
505 to significantly accelerate the flow, we find that exceptionally high initial pore fluid pressure is
506 required to overcome the resisting stresses. Final flow thicknesses for flows starting with
507 different ratios of initial pore fluid pressure to basal normal stress (λ) are shown in Figures 5c
508 (for collapse fed flows) and 5d (for fountain fed flows). There is minimal flow front propagation
509 even with λ=0.90 initially. High initial pore fluid pressure to basal normal stress ratio values of
510 $\lambda > 0.95$ are required to achieve significant 'downslope' movement on the flanks of Venusian
511 shields and coronae that have slopes averaging ¿2°.

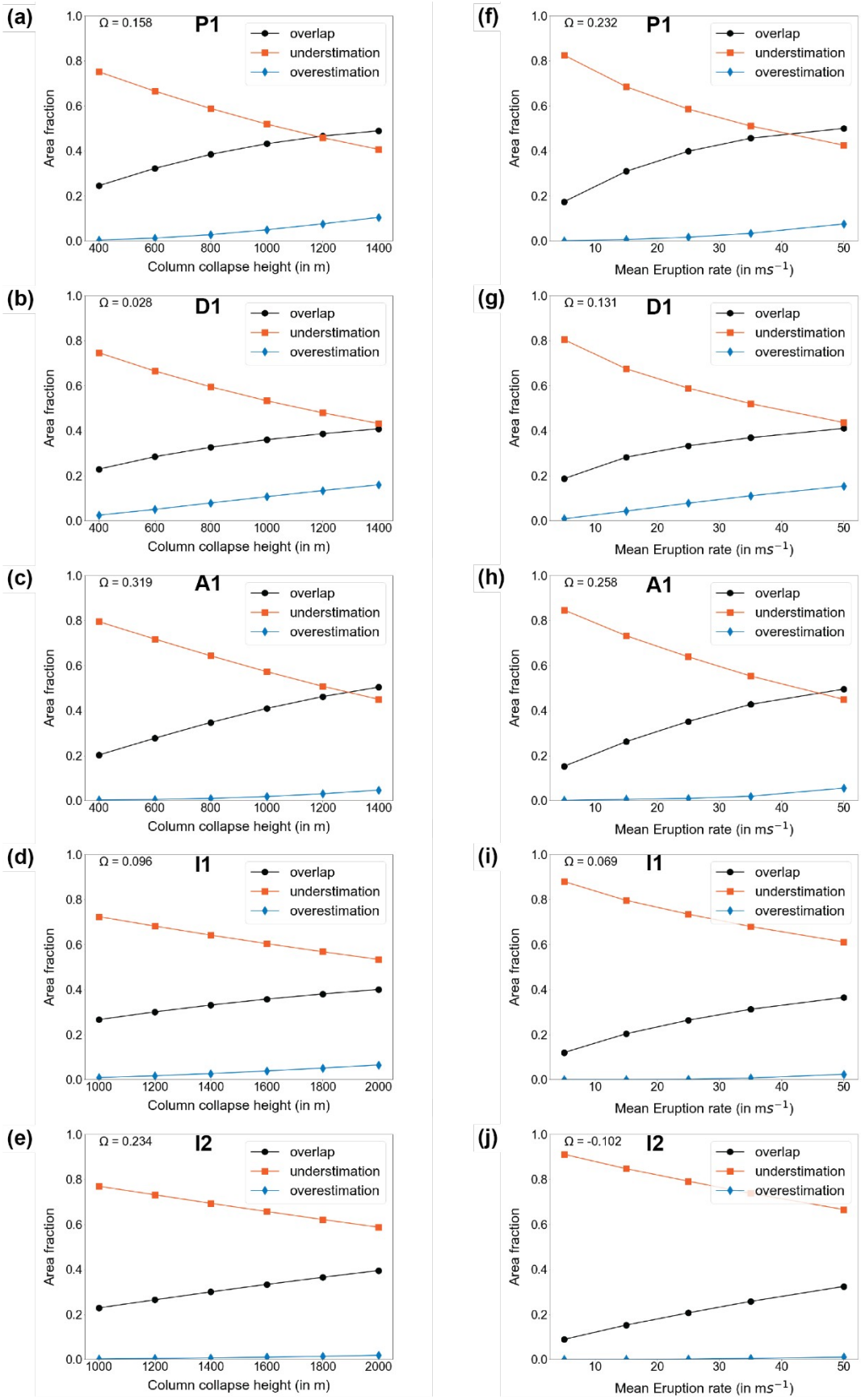
(a)
Ω = 0.158
P1
(b)
Ω = 0.028
D1
(c)
Ω = 0.319
A1
(d)
Ω = 0.096
I1
(e)
Ω = 0.234
I2
(f)
Ω = 0.232
P1
(g)
Ω = 0.131
D1
(h)
Ω = 0.258
A1
(i)
Ω = 0.069
I1
(j)
Ω = -0.102
I2
overlap
understimation
overestimation
Area fraction
Column collapse height (in m)
Mean Eruption rate (in ms^{-1})

Figure 6. Plots summarizing the comparison between modeled and observed pyroclastic deposits (P1, D1, A1, I1 and I2) using the approach in Heiser *et al.* (2017). (a)-(e) Results for collapse-fed flows are plotted as a function of column heights. Note that panels for the deposits P1, D1 and A1, respectively have a different x-axis range than panels for deposits I1 and I2, respectively. (f)-(j) Results for fountain-fed flows are plotted as a function of mean eruption rate. For deposits P1, D1 and A1, reasonable match between the mapped and the modeled deposit extent is achieved at higher collapse heights or larger eruption rates. All model results substantially underestimate the true deposit area for deposits I1 and I2. The highest similarity indices obtained for each deposit and initiation style corresponding to the model inputs in Table 2 are shown in the top left of each panel.

4.4 Best fit model parameters from similarity index calculations

The α (overlap), β(underestimation), and γ (overestimation) values as a function of collapse height for column collapse initiation are plotted in Figures 6a to 6e. Similar plots are shown for the case of fountain initiation in Figures 6f to 6j. Only results from simulations using initial $\lambda = 0.99$, are shown in Figure 6. The percentage overlap is considerably smaller for all other initial values of λ(¿0.90, 0.95, 0.98). Note that maximum overlap between the modeled and observed deposit is achieved for the upper range of collapse heights and eruption rates used in our simulations, indicating that most of our model results consistently underestimate the actual pyroclastic deposit area. The percentage area underestimated remains greater than the percentage deposit area reproduced for collapse heights < 1200-1400 m and for eruption rates < 50 ms^{-1} for the smaller deposits P1, D1 and A1 (Figures 4a-4c and 4f-4h). None of our simulations result in a scenario where the deposit area reproduced is greater than the deposit area underestimated for the large deposits on the flanks of Irnini Mons (Figures 4d, 4e, 4i, and 4j). The modeled final deposit volume corresponding to the best fit simulations are reported in Table 2. The modeled volume ranges from 140 km^3 to 280 km^3 for P1, D1 and A1; for the larger deposits I1 and I2, the models show volumes as large as ~780 km^3.

5 Discussion

5.1 Impulsive collapse vs sustained fountaining initiation: implications for flow thickness and duration

The two styles of pyroclastic flow initiation explored by our models – collapse and fountaining – emplace material in different ways resulting in different deposit extents. This is reflected in the estimated similarity indices Ω and the percentage overlaps in area between the mapped and the modeled deposits extents (Figure 4 and Table 2). Deposits P1 and D1 in Eastern Eistla Regio show higher Ω and percentage overlap in area for emplacement by fountain-fed flows; whereas collapse initiation results in better Ω and percentage overlap in area for the Western Eistla Regio deposits (A1, I1 and I2).The differences in these computed metrics (shown in Table 2) are only slightly different for the two geographic groups of deposits and can be explained by the uncertainties in the initial conditions; this precludes making any inferences about the more likely style of PDC initiation for each deposit. In general, the low percentage overlap in area between the mapped and modeled deposit extents for small collapse heights and fountaining rates (Figure 6) show that both types of initiation severely underestimate the deposit extent for small volume flows with low initial pore fluid pressure. Highly fluidized, large volume flows would be necessary to realize the large deposit extent. Our models show that large collapse heights for column collapse initiation, and large eruption rate (or fountain height) for fountaining initiation can produce flows capable of achieving large extents and runout distances (Figure 5a and 5b) resulting in deposits similar to the proposed pyroclastic flow deposits investigated here.

While it is not possible to deduce which style of initiation is more likely, the model suggests there would be quantitative differences in deposit properties, such as deposit thickness and total volume, that could be used to differentiate between the different initiation styles given higher resolution observations. As an example, we use the model results corresponding to the best-fit model parameters for deposit P1 to explore these differences. The DEM for this location, shown in Figure 7a, comprises both high resolution stereo-SAR data and coarser resolution Magellan altimetry data stitched together. Figures 7c and 7d show map views of the final flow thickness for collapse-fed and fountain-fed flows that resulted in the highest similarity index, respectively. The runout and extent of a smaller volume collapse-fed flow ($168\,km^3$ volume) is equivalent to the runout and extent of a more voluminous fountain-fed flow ($400\,km^3$ volume). This

difference in total volume is accommodated as a change in the final deposit thickness between the two styles of initiation. The deposit from the fountain-fed flow, while exhibiting runout distances similar to the collapse-fed flow, has a mean thickness of 55 ± 35 m which is nearly 3 times the mean thickness of the collapse fed flow (20 ± 11.8 m). The spatial distribution of the final deposit thickness is also different between the two styles of initiation. The collapse-fed flows show a thinning trend away from the source whereas the fountain-fed flows show relatively uniform thickness for most part of the deposit (see Figures 5a and 5b). Both types of flows come to rest by abrupt arrest in our models, resulting in flow margin thicknesses much greater than 1 – 2 meters. Margin thickness greater than a couple of meters is irreconcilable with the diffuse deposit boundaries observed in the SAR images. Diffuse boundaries are expected to arise when the upper unit is thin enough at the margins to allow return echoes from the underlying substrate; it is unlikely that the 12.6 cm wavelength Magellan SAR will be able to "see through" margins >2 m thick. There are two possible explanations for this disparity: (1) the boundaries of the deposits have been eroded and reworked into a thin mantle adjacent to the deposit or 2) the pyroclastic flow that emplaced these deposits had an upper dilute component with longer runouts than the dense basal portion.

The flow duration and velocity for the two initiation mechanisms also differ significantly. Figure 7e shows the progression of flow velocity and runout distance as a function of simulation time, highlighting the differences in the duration of emplacement between the two initiation styles. The energy stored in 0.4-2 km tall columns (the range of column heights modeled) is available as kinetic energy for the pyroclastic flow generated via collapse. This leads to flows that are faster than those generated by low fountaining (maximum fountain height of 50 m used in the model). We see that the collapse-generated flow starts out with much higher initial velocity which causes the flow to travel farther than the fountain-fed flow and halt quickly within the first 400 s of the simulation (black curves in Figure 7e). On the other hand, the fountain-fed flow shows very low initial velocity which is maintained until the fountaining stops at t=400 s (black curve with triangle markers in Figure 7e). After the fountain ends, the flow begins to decelerate. This flow keeps moving for about 600 s after the end of fountaining, coming to rest at nearly the same distance from the source as the collapse fed flow. The difference in flow dynamics for the two styles of initiation discussed above can be used as a first-order approach to constrain the properties of parent pyroclastic flows of the small deposits P1, D1 and A1. If these deposits were

formed from a collapsing column, then the parent flow was likely fast, short-lived (< 6 min) and deposited pyroclastic material ~20 m thick. Alternatively, if the pyroclastic flow that emplaced these deposits resulted from low fountaining, the resulting deposits could be up to ~70 m thick in some places. The fountain-fed flow would have been comparatively slower and longer-lived. For deposit P1, the modeled flow lasts > 10 min after the end of a fountaining episode lasting 400 s (see Figure 7e); flows resulting from fountaining eruptions lasting longer would have even longer flow durations. The large deposits I1 and I2 on the flanks of Irnini Mons are not well reproduced by our simulations indicating that larger flow velocities (and hence a turbulent flow component) would have been necessary to emplace deposits with such enormous spatial extents. Higher eruption column heights and larger eruption rates, which could be possible on Venus under a narrow range of volatile contents and atmospheric conditions (Glaze, 1999; Glaze *et al.*, 2011; Airey *et al.*, 2015), could have been involved in emplacing units I1 and I2. The dynamics of such high velocity, turbulent flows under Venus's conditions are currently being investigated by the authors.

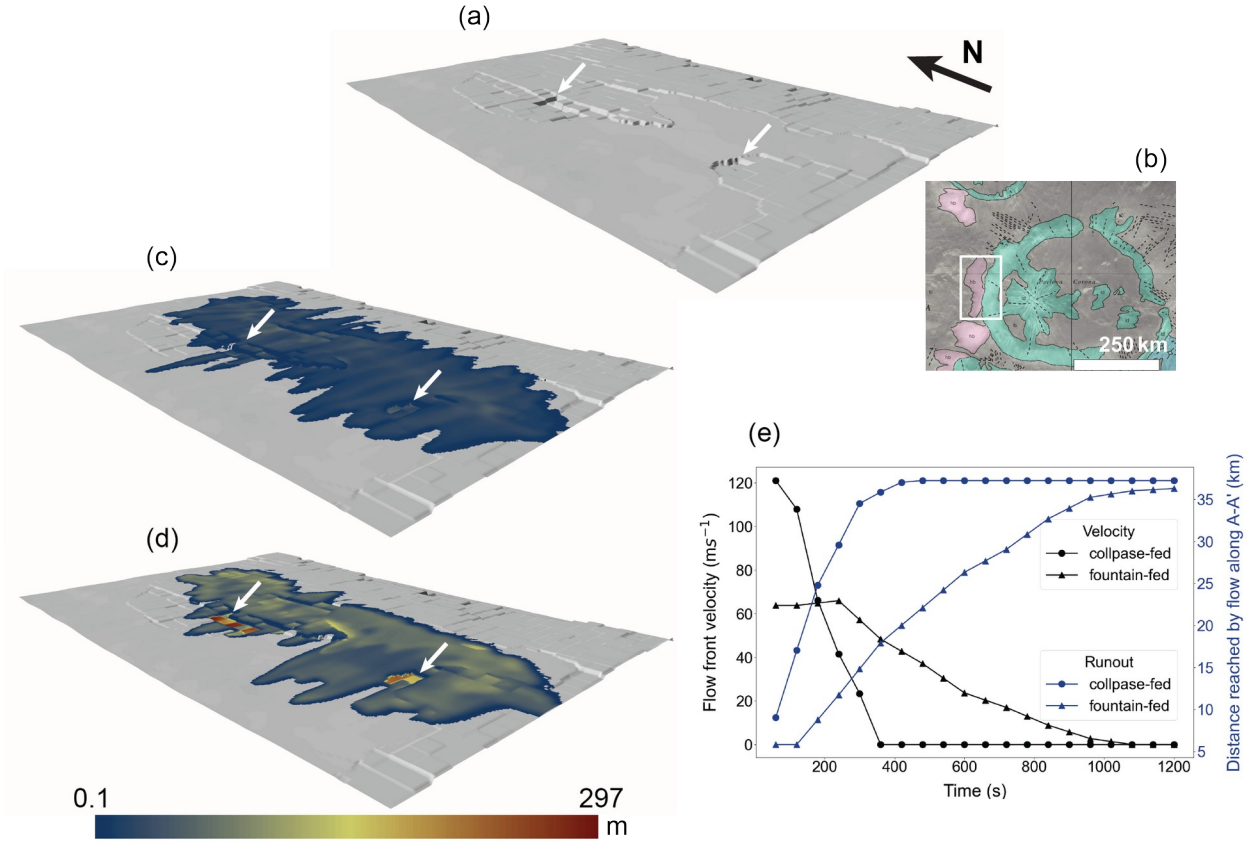

Figure 7. (a) Three-dimensional perspective view of a hillshade map of study site P1 (vertical exaggeration = 3x). (b) Geological map of Pavlova Corona overlaid on top of Magellan SAR image. The white rectangle marks the bounds of the hillshade maps shown in (a), (c) and (d); pink – proposed pyroclastic units, green – densely lineated material. (c) Final 2D flow thickness maps for impulsive collapse initiation overlaid on the hillshade map. (d) Final 2D flow thickness maps for sustained fountaining initiation overlaid on the hillshade map. Final flow thickness for the fountain-fed flow is noticeably higher than the final thickness for the collapse-fed flow. White arrows in (a), (c) and (d) point to examples of locations where the high-resolution stereo-SAR DEM has been stitched together with coarser resolution Magellan altimetry data, resulting in artifacts in the DEM used. Unusually high values of flow thickness can be seen at these locations for both collapse and fountaining initiations. (e) Plot showing the evolution of velocity (in black) and flow runout (in blue) as a function if simulation time. Note the higher initial velocity as well as quick deceleration for collapse fed flow (black curve with circle markers) relative to the velocity and deceleration seen for fountain-fed flow (black curve with triangle markers). The collapse-fed flows reach the final runout distances sooner (blue curve with circle markers) in comparison to the slow-moving fountain fed flows (blue curve with triangle markers).

5.2 Dense pyroclastic flows on shallow slopes: implications for pyroclastic flow dynamics on Venus

The proposed pyroclastic deposits on Venus occur near volcanic landscapes with low topographic slopes consistent with dominantly mafic volcanism. Pyroclastic flows produced by mafic volcanism are less common on Earth (examples include Freundt and Schmincke, 1995; Robin *et al.*, 1995; Allen, 2004; Giordano *et al.*, 2006). The more typical case of silicic pyroclastic flows occurs on steep-sided stratocones. Such flows released onto steep topography immediately undergo acceleration before eventually attaining a constant velocity phase (Roche *et al.*, 2008; Gueugneau *et al.*, 2017). Any acceleration or deceleration after this initial stage is induced by changes in the basal topography. To keep the flow in motion, either slope angles greater than the basal friction angle or pore fluid pressure large enough to overcome basal friction is required. The topographic slope at all the deposits studied here has a mean value < 2°. Consequently, the likelihood of topography-induced acceleration in the flow once past the initial

stage is negligible. The resulting implications for long runouts of pyroclastic flows on shallow slopes are discussed below.

1. For emplacing large-scale deposits over relatively shallow slopes on Venus, fluidization of pyroclastic flows via excess pore fluid pressure is a key characteristic. In the absence of steep slopes or positive breaks in topography that can accelerate the flow, fluidization provides a means to minimize the resisting stresses and sustain flow velocity for long distances. Our models show that very high initial interstitial pore pressures (> 95% of the total normal stress, see section 4.3) is needed to transport the flows across distances >60 km at our study sites. This is consistent with findings that pyroclastic flows that travel down gentle slopes only do so when a pore-pressure induced fluidized layer develops (Takahashi and Tsujimoto, 2000). For flows formed from magmas with high gas content and for thick flows, pore-pressure induced fluidization can be achieved by mechanisms such as movement of gas from the substrate upwards into the current, upward escape of air trapped beneath the flow front, and exsolution of gas from hot pyroclasts (Sparks, 1978; Walker, Wilson, *et al.*, 1980; Branney and Kokelaar, 2002). If (1) the size distribution of solid particles comprising the flow was small enough to allow for very slow dissipation of pore fluid pressure and/or (2) the entrainment of air causing the flow to inflate is negligible, high pore fluid pressure can be maintained for longer times.
2. The modeled flow travels at velocities equal to or less than the initial velocity for most of its flow duration (black curves in Figure 7e). Unusually high flow velocities are observed only at locations where the stereo DEM has been stitched together with altimetry DEM values. While turbulent transport could be possible in proximal areas when the flow still has high velocity (particularly for the flows fed by columns collapsing from a few kilometers height), it is unlikely that the flow will subsequently develop turbulence during later stages of emplacement along gentle slopes. Deflation of the flow caused by the diffusion of pore pressure also acts to keep the flow laminar (Sheridan, 1979; Druitt, 1998). Therefore, low fountains and small columns modeled in this study are expected to result in deflated, ground-hugging flows that travel in a laminar fashion.

5.3 Large volume PDC deposits on Venus: a comparison with terrestrial ignimbrites

The simulation results presented here suggest that the proposed pyroclastic deposits investigated on Venus are large volume deposits (310 – 780 km^3 bulk volume for the large deposits at Irnini Mons and $140-280\,km^3$ bulk volume for the other smaller deposits), with mean thickness ranging from 20 – 70 m. Erosion and elutriation of fine ash could have resulted in actual deposit volumes less than the predicted volumes. Since no redeposited pyroclastic material or co-ignimbrite ash, which could aid in more accurate volume estimates, have been identified close to the study sites, the modeled deposit volume provides the closest estimate of the true deposit volume. Eruptions capable of emplacing such voluminous deposits would fall close to the lower end of terrestrial super-eruptions not observed in historic or recent times, where the total magma discharge exceeds $450\,km^3$ DRE (Sparks *et al.*, 2005; Self, 2006). Some of the largest known ashflow deposits of felsic composition on Earth include the Campanian ignimbrite (~$500\,km^3$ bulk volume, Fisher *et al.* (1993)), Bishop tuff ¿ bulk volume, Hildreth and Mahood (1986)), Fish Canyon tuff (~$500\,km^3$ bulk volume, Lipman *et al.* (1973)), Peach spring tuff (>$1300\,km^3$ DRE (dense rock equivalent), Ferguson *et al.* (2013)), Taupo ignimbrites (~$500\,km^3$ bulk volume, Wilson (1985)) and Rattlesnake tuff (~$280 km^3$ DRE, Streck and Grunder (1995)). The modeled deposit volumes greatly exceed the volumes of less common terrestrial mafic ignimbrites such as Halarauður ignimbrite (¿$20\,km^3$ bulk volume, Rooyakkers *et al.*, 2020), the Okmok PDC deposits ($29\,km^3$ DRE, Burgisser, 2005), and Villa Senni ignimbrite ($30\,km^3$ DRE, Watkins *et al.*, 2002).

The final thickness of the deposits predicted by the dense pyroclastic flow models (~20-70 m mean thickness) is in contradiction with previous interpretations of the Venusian units as thin, 'mantling' deposits with thickness ranging from tens of centimeters to a few meters (McGill, 2000; Grosfils et al., 2011). The thin, mantling interpretation for the Venus deposits is perhaps most comparable to terrestrial ignimbrites that are deposited as a veneer not more than a few meters thick (termed low aspect ratio ignimbrites (LARI) by Walker, Heming, *et al.* (1980)). While our models predict deposits thicker than the ignimbrite veneers, the low thicknesses inferred from the model relative to the deposit area yields an aspect ratio close to some of the well-studied LARIs such as the Campanian ignimbrite (Fisher *et al.*, 1993), Kizilkaya ignimbrite (Schumacher and Mues-Schumacher, 1996), and the Villa Senni ignimbrite (Watkins *et al.*,

2002; Giordano *et al.*, 2006). LARIs were originally thought to form only from high-velocity, turbulent flows generated by the collapse of an extraordinarily high eruption column (>50 km high), which allow for long runouts (Walker, Heming, *et al.*, 1980; Wilson, 1985). More recently, Cas *et al.* (2011) showed that LARIs can also be deposited from fluidized, fines-rich, nonturbulent flows that travel across gently sloping terrain (8°-9° slope) at very low velocities (< 10 ms^{-1}). These flows are generated not from tall eruption columns but from low fountaining-style eruptions with high discharge rates (similar to the fountaining initiation considered in this study). Our simulations of dense particle-laden flows fed by sustained fountaining on Venus are mostly analogous to such low-energy LARI emplacement. The slightly higher flow velocities (see Figure 7e) and deposit thicknesses (see Figure 5b) seen in our models can be explained by uncertainties in the interaction of the flow with underlying topography, caused by limitations in the topography dataset. Our impulsive collapse initiation model is in discord with low-energy LARI emplacement due to relatively larger initial flow velocities (~ 100 ms^{-1}, also see Figure 7e); this is suggestive of a turbulent flow in the proximal stages of emplacement.

6 Conclusions

Large deposits with high radar return echoes on the summits of Irnini Mons and Anala Mons, and on the flanks of Didilia Corona and Pavlova Corona have been proposed to be pyroclastic flow deposits. These units have high CPR interpreted to be caused by extensive centimeter-sized clasts embedded in the deposits. Larger clasts are typically transported as a particle-laden, dense pyroclastic density current. In this study, we model the transport of dense pyroclastic flows using a 2D depth-averaged mass flow model to determine the physical properties of PDCs that could have resulted in the emplacement of the proposed pyroclastic units. Flows generated by impulsive collapse of small columns and long-lived fountains, both of which are plausible under Venus's ambient conditions, were simulated. Multiple linear vents of equal length, in accordance with the expected vent dimensions at ring fracture systems, were used. Such spatially distributed sources are necessary to reproduce the observed lateral extent of deposits. Due to low mean slopes (<2°) at our study sites, simulations indicate that fluidization of pyroclastic flows via high pore pressure is critical for reproducing the extensive deposits. The low topographic slope also acts to prevent development of turbulence in the later stages of the flow. The deposits on the flanks of Irnini Mons are relatively large and not well reproduced by our models. More energetic

734 pyroclastic flows formed by the collapse of exceptionally tall columns may be capable of
735 emplacing such deposits. Such large column forming eruptions have been predicted to occur at
736 high altitude and high latitude regions on Venus; but it is unclear whether such eruptions are
737 possible at Irnini Mons. The dynamics of large, turbulent flows and their interactions with
738 Venus's atmosphere are the subject of ongoing studies by the authors. Our models show that
739 collapse of columns >1.2 – 1.4 km tall from linear vents with widths ~ 1 km could give rise to
740 the observed spatial extent of the smaller deposits on the flanks of Pavlova Corona, Didilia
741 Corona and Anala Mons. Similarly, fountains of height ~50 m lasting longer than 400s could
742 also give rise to long runout pyroclastic flows that could have emplaced the observed deposits at
743 these locations. While both impulsive collapse and fountaining could have resulted in the
744 observed deposit extent, there are significant differences in the flow dynamics between these two
745 scenarios that lead to modeled deposits with different structures. Simulations suggest that
746 deposits resulting from discrete collapses are expected to be a few tens of meters thick; they
747 likely form from fast-moving flows (< 6 min). Fountain-fed flows, on the other hand, are
748 expected to be comparatively slow-moving and long-lasting, similar to low-energy LARI
749 emplacement on Earth. They result in thicker deposits than collapse-fed flows. Given the
750 resolution limitations of the current dataset, deposits formed by these two mechanisms would be
751 indistinguishable. Higher resolution imaging and topography data from proposed missions like
752 EnVision (Ghail *et al.*, 2018) and VERITAS (Smrekar *et al.*, 2016) would aid in constraining the
753 vent locations and the deposit thicknesses; this could be used to further refine the model's initial
754 conditions, allowing for more detailed model simulations of pyroclastic flow transport on
755 Venus's surface.

756 **Acknowledgments, Samples, and Data**

757 This study was supported by FINESST grant 80NSSC19K1540 to I. Ganesh and SSW grant
758 80NSSC20K1040 to L. M. Carter. The Venus Magellan SAR FMAP Left Look Global Mosaic
759 75m v1 data set used for mapping was obtained from the Planetary Data System (PDS) and
760 processed using USGS Astrogeology Science Center's Map-A-Planet 2. The stereo SAR
761 topography data used as input to the model can be found at
762 https://sites.google.com/alaska.edu/robertherrick/resources/stereo-derived-topography-for-
763 venus?authuser=0. The 2D pyroclastic flow model used is available through GitHub and

CSDMS at https://doi.org/10.5281/zenodo.4724233. Computations were performed on the University of Arizona's TAPIR lab cluster maintained by Michael Christoffersen, and High Performance Computing (HPC) Ocelote cluster maintained by the University of Arizona Research Technologies department.

References

Airey, M. W., Mather, T. A., Pyle, D. M., Glaze, L. S., Ghail, R. C. and Wilson, C. F. (2015) 'Explosive volcanic activity on Venus: The roles of volatile contribution, degassing, and external environment', *Planetary and Space Science*. Pergamon, 113–114, pp. 33–48. doi: 10.1016/J.PSS.2015.01.009.

Allen, S. R. (2004) 'Complex spatter- and pumice-rich pyroclastic deposits from an andesitic caldera-forming eruption: The Siwi pyroclastic sequence, Tanna, Vanuatu', *Bulletin of Volcanology*. Springer, 67(1), pp. 27–41. doi: 10.1007/s00445-004-0358-6.

Branney, M. J. and Kokelaar, P. (1992) 'A reappraisal of ignimbrite emplacement: progressive aggradation and changes from particulate to non-particulate flow during emplacement of high-grade ignimbrite', *Bulletin of Volcanology*. Springer-Verlag, 54(6), pp. 504–520. doi: 10.1007/BF00301396.

Branney, M. J. and Kokelaar, P. (2002) 'Pyroclastic Density Currents and the Sedimentation of Ignimbrites', *Geological Society, London, Memoirs*, 27(1).

Burgisser, A. (2005) 'Physical volcanology of the 2,050 BP caldera-forming eruption of Okmok volcano, Alaska', *Bulletin of Volcanology*. Springer, 67(6), pp. 497–525. doi: 10.1007/s00445-004-0391-5.

Bursik, M. I. and Woods, A. W. (1996) 'The dynamics and thermodynamics of large ash flows', *Bulletin of Volcanology*. Springer Verlag, 58(2–3), pp. 175–193. doi: 10.1007/s004450050134.

Campbell, B. A. (1994) 'Merging Magellan Emissivity and SAR Data for Analysis of Venus Surface Dielectric Properties', *Icarus*. Academic Press, 112(1), pp. 187–203. doi: 10.1006/ICAR.1994.1177.

Campbell, B. A. and Campbell, D. B. (1992) 'Analysis of volcanic surface morphology on Venus from comparison of Arecibo, Magellan, and terrestrial airborne radar data', *Journal of Geophysical Research*, 97(E10), p. 16293. doi: 10.1029/92JE01558.

Campbell, B. A., Morgan, G. A., Whitten, J. L., Carter, L. M., Glaze, L. S. and Campbell, D. B.

(2017) 'Pyroclastic flow deposits on Venus as indicators of renewed magmatic activity', *Journal of Geophysical Research: Planets*, 122(7), pp. 1580–1596. doi: 10.1002/2017JE005299.

Campbell, B. and Clark, D. (2006) 'Geologic map of the Mead quadrangle (V-21), Venus', *US Geological Survey Scientific Investigations Map 2897*. doi: doi.org/10.3133/sim2897.

Cas, R. A. F., Wright, H. M. N., Folkes, C. B., Lesti, C., Porreca, M., Giordano, G. and Viramonte, J. G. (2011) 'The flow dynamics of an extremely large volume pyroclastic flow, the 2.08-Ma Cerro Galán Ignimbrite, NW Argentina, and comparison with other flow types', *Bulletin of Volcanology*, 73(10), pp. 1583–1609. doi: 10.1007/s00445-011-0564-y.

Dade, W. B. and Huppert, H. E. (1995a) 'A box model for non-entraining, suspension-driven gravity surges on horizontal surfaces', *Sedimentology*, 42(3), pp. 453–470. doi: 10.1111/j.1365-3091.1995.tb00384.x.

Dade, W. B. and Huppert, H. E. (1995b) 'Runout and fine-sediment deposits of axisymmetric turbidity currents', *Journal of Geophysical Research*, 100(C9). doi: 10.1029/95jc01917.

Dade, W. B. and Huppert, H. E. (1996) 'Emplacement of the Taupo ignimbrite by a dilute turbulent flow', *Nature*, 381(6582), pp. 509–512. doi: 10.1038/381509a0.

Denlinger, R. P. and Iverson, R. M. (2001) 'Flow of variably fluidized granular masses across three-dimensional terrain: 2. Numerical predictions and experimental tests', *Journal of Geophysical Research: Solid Earth*. American Geophysical Union (AGU), 106(B1), pp. 553–566. doi: 10.1029/2000jb900330.

Denlinger, R. P. and Iverson, R. M. (2004) 'Granular avalanches across irregular three-dimensional terrain: 1. Theory and computation', *Journal of Geophysical Research: Earth Surface*, 109(F1). doi: 10.1029/2003JF000085.

Dombard, A. J., Johnson, C. L., Richards, M. A. and Solomon, S. C. (2007) 'A magmatic loading model for coronae on Venus', *Journal of Geophysical Research*, 112(E4), p. E04006. doi: 10.1029/2006JE002731.

Druitt, T. H. (1998) 'Pyroclastic density currents', in Gilbert, J. S. and Sparks, R. S. J. (eds) *The Physics of Explosive Volcanic Eruptions*. 1st edn. Geological Society, London, Special Publications, pp. 145–182.

Druitt, T. H., Avard, G., Bruni, G., Lettieri, P. and Maez, F. (2007) 'Gas retention in fine-grained pyroclastic flow materials at high temperatures', *Bulletin of Volcanology*. Springer, 69(8), pp. 881–901. doi: 10.1007/s00445-007-0116-7.

825 Druitt, T. H., Bruni, G., Lettieri, P. and Yates, J. G. (2004) 'The fluidization behaviour of
826 ignimbrite at high temperature and with mechanical agitation', *Geophysical Research Letters*.
827 American Geophysical Union, 31(2). doi: 10.1029/2003GL018593.
828 Dufek, J. (2016) 'The Fluid Mechanics of Pyroclastic Density Currents', *Annual Review of Fluid*
829 *Mechanics*. Annual Reviews, 48(1), pp. 459–485. doi: 10.1146/annurev-fluid-122414-034252.
830 Esposito, L. W. (1984) 'Sulfur dioxide: Episodic injection shows evidence for active Venus
831 volcanism', *Science*. American Association for the Advancement of Science, 223(4640), pp.
832 1072–1074. doi: 10.1126/science.223.4640.1072.
833 Fagents, S. A. and Wilson, L. (1995) 'Explosive volcanism on Venus: Transient volcanic
834 explosions as a mechanism for localized pyroclast dispersal', *Journal of Geophysical Research-*
835 *Planets*, 100(E12), pp. 26327–26338. doi: 10.1029/95je03202.
836 Ferguson, C. A., McIntosh, W. C. and Miller, C. F. (2013) 'Silver Creek caldera-The tectonically
837 dismembered source of the Peach Spring Tuff', *Geology*. GeoScienceWorld, 41(1), pp. 3–6. doi:
838 10.1130/G33551.1.
839 Fink, J. H., Bridges, N. T. and Grimm, R. E. (1993) 'Shapes of Venusian "pancake" domes
840 imply episodic emplacement and silicic composition', *Geophysical Research Letters*. Wiley-
841 Blackwell, 20(4), pp. 261–264. doi: 10.1029/92GL03010.
842 Fisher, R. V. (1966) 'Mechanism of deposition from pyroclastic flows', *American Journal of*
843 *Science*. American Journal of Science (AJS), 264(5), pp. 350–363. doi: 10.2475/ajs.264.5.350.
844 Fisher, R. V., Orsi, G., Ort, M. and Heiken, G. (1993) 'Mobility of a large-volume pyroclastic
845 flow - emplacement of the Campanian ignimbrite, Italy', *Journal of Volcanology and*
846 *Geothermal Research*. Elsevier, 56(3), pp. 205–220. doi: 10.1016/0377-0273(93)90017-L.
847 Freundt, A. and Schmincke, H. U. (1995) 'Eruption and emplacement of a basaltic welded
848 ignimbrite during caldera formation on Gran Canaria', *Bulletin of Volcanology*. Springer-Verlag,
849 56(8), pp. 640–659. doi: 10.1007/BF00301468.
850 Ganesh, I., McGuire, L. A., Carter, L. M. (2020). PyDeCe: First release of PyDeCe (Version
851 v1.0). Zenodo. http://doi.org/10.5281/zenodo.4724233
852 Garvin, J. B., Head, J. W. and Wilson, L. (1982) 'Magma vesiculation and pyroclastic volcanism
853 on Venus', *Icarus*. Academic Press, 52(2), pp. 365–372. doi: 10.1016/0019-1035(82)90119-1.
854 George, D. L. and Iverson, R. M. (2014) 'A depth-averaged debris-flow model that includes the
855 effects of evolving dilatancy. II. Numerical predictions and experimental tests', *Proceedings of*

856 *the Royal Society A: Mathematical, Physical and Engineering Sciences*. Royal Society of
857 London, 470(2170). doi: 10.1098/rspa.2013.0820.
858 Ghail, R. C., Hall, D., Mason, P. J., Herrick, R. R., Carter, L. M. and Williams, E. (2018)
859 'VenSAR on EnVision: Taking earth observation radar to Venus', *International Journal of*
860 *Applied Earth Observation and Geoinformation*. Elsevier B.V., 64, pp. 365–376. doi:
861 10.1016/j.jag.2017.02.008.
862 Ghail, R. C. and Wilson, L. (2015) 'A pyroclastic flow deposit on Venus', *Geological Society,*
863 *London, Special Publications*. Geological Society of London, 401(1), pp. 97–106. doi:
864 10.1144/sp401.1.
865 Giordano, G., De Benedetti, A. A., Diana, A., Diano, G., Gaudioso, F., Marasco, F., Miceli, M.,
866 Mollo, S., Cas, R. A. F. and Funiciello, R. (2006) 'The Colli Albani mafic caldera (Roma, Italy):
867 Stratigraphy, structure and petrology', *Journal of Volcanology and Geothermal Research*.
868 Elsevier, 155(1–2), pp. 49–80. doi: 10.1016/j.jvolgeores.2006.02.009.
869 Glaze, L. S. (1999) 'Transport of SO 2 by explosive volcanism on Venus', *Journal of*
870 *Geophysical Research: Planets*, 104(E8), pp. 18899–18906. doi: 10.1029/1998JE000619.
871 Glaze, L. S., Baloga, S. M. and Wimert, J. (2011) 'Explosive volcanic eruptions from linear
872 vents on Earth, Venus, and Mars: Comparisons with circular vent eruptions', *Journal of*
873 *Geophysical Research*, 116(E1), p. E01011. doi: 10.1029/2010JE003577.
874 Grosfils, E. B., Long, S. M., Venechuk, E. M., Hurwitz, D. M., Richards, J. W., Brian, K.,
875 Dorothy E., D. and Hardin, J. (2011) 'Geologic Map of the Ganiki Planitia Quadrangle (V-14),
876 Venus', *U.S. Geological Survey Scientific Investigations Map 3121*.
877 Gueugneau, V., Kelfoun, K., Roche, O. and Chupin, L. (2017) 'Effects of pore pressure in
878 pyroclastic flows: Numerical simulation and experimental validation', *Geophysical Research*
879 *Letters*, 44(5), pp. 2194–2202. doi: 10.1002/2017GL072591.
880 Hallworth, M. A. and Huppert, H. E. (1998) 'Abrupt transitions in high-concentration, particle-
881 driven gravity currents', *Physics of Fluids*, 10, p. 1083. doi: 10.1063/1.869633.
882 Head, J. W., Campbell, D. B., Elachi, C., Guest, J. E., Mckenzie, D. P., Saunders, R. S., Schaber,
883 G. G. and Schubert, G. (1991) 'Venus Volcanism: Initial Analysis from Magellan Data', *Science*.
884 American Association for the Advancement of Science, 252(5003), pp. 276–288. doi:
885 10.1126/science.252.5003.265.
886 Head, J. W., Crumpler, L. S., Aubele, J. C., Guest, J. E. and Saunders, R. S. (1992) 'Venus

887 volcanism: Classification of volcanic features and structures, associations, and global distribution
888 from Magellan data', *Journal of Geophysical Research*, 97(E8), p. 13153. doi:
889 10.1029/92JE01273.
890 Head, J. W. and Wilson, L. (1982) 'Volcanic Processes on Venus', in *Lunar and Planetary*
891 *Science XIII*, pp. 312–313.
892 Head, J. W. and Wilson, L. (1986) 'Volcanic processes and landforms on Venus: Theory,
893 predictions, and observations', *Journal of Geophysical Research*, 91(B9), pp. 9407–9446. doi:
894 10.1029/JB091iB09p09407.
895 Heiser, M., Scheidl, C. and Kaitna, R. (2017) 'Evaluation concepts to compare observed and
896 simulated deposition areas of mass movements', *Computational Geosciences*. Springer
897 International Publishing, 21(3), pp. 335–343. doi: 10.1007/s10596-016-9609-9.
898 Herrick, R. R., Stahlke, D. L. and Sharpton, V. L. (2012) 'Fine-scale Venusian topography from
899 Magellan stereo data', *Eos, Transactions American Geophysical Union*, 93(12), pp. 125–126.
900 doi: 10.1029/2012EO120002.
901 Hildreth, W. and Mahood, G. A. (1986) 'Ring-fracture eruption of the Bishop Tuff (USA).',
902 *Geological Society of America Bulletin*. GeoScienceWorld, 97(4), pp. 396–403. doi:
903 10.1130/0016-7606(1986)97<396:REOTBT>2.0.CO;2.
904 Holohan, E. P., Troll, V. R., va Wyk de Vries, B., Walsh, J. J. and Walter, T. R. (2008)
905 'Unzipping long valley: An explanation for vent migration patterns during an elliptical ring
906 fracture eruption', *Geology*. GeoScienceWorld, 36(4), pp. 323–326. doi: 10.1130/G24329A.1.
907 Iverson, R. M. and Denlinger, R. P. (2001) 'Flow of variably fluidized granular masses across
908 three-dimensional terrain: 1. Coulomb mixture theory', *Journal of Geophysical Research: Solid*
909 *Earth*, 106(B1), pp. 537–552. doi: 10.1029/2000JB900329.
910 Jessop, D. E., Gilchrist, J., Jellinek, A. M. and Roche, O. (2016) 'Are eruptions from linear
911 fissures and caldera ring dykes more likely to produce pyroclastic flows?', *Earth and Planetary*
912 *Science Letters*. Elsevier B.V., 454, pp. 142–153. doi: 10.1016/j.epsl.2016.09.005.
913 Jop, P., Forterre, Y. and Pouliquen, O. (2006) 'A constitutive law for dense granular flows',
914 *Nature*. Nature Publishing Group, 441(7094), pp. 727–730. doi: 10.1038/nature04801.
915 Keddie, S. T. and Head, J. W. (1995) 'Formation and evolution of volcanic edifices on the Dione
916 Regio rise, Venus', *Journal of Geophysical Research*, 100(E6), p. 11729. doi:
917 10.1029/95JE00822.

Kelfoun, K. and Druitt, T. H. (2005) 'Numerical modeling of the emplacement of Socompa rock avalanche, Chile', *Journal of Geophysical Research*, 110(B12), p. B12202. doi: 10.1029/2005JB003758.

Lipman, P. W., Steven, T. A., Luedke, R. G. and Burbank, W. (1973) 'Revised volcanic history of the San Juan, Uncompahgre, Silverton, and Lake City calderas in the western San Juan Mountains, Colorado', *Journal of Research of the U.S. Geological Survey*, 1(6).

McGill, G. (2000) 'Geologic map of the Sappho Patera quadrangle (V-20), Venus', *US Geological Survey Scientific Investigations Map 2637*. doi: doi.org/10.3133/i2637.

McGill, G. E. (1998) 'Venus: Evolution of Central Eistla Regio', in *29th Annual Lunar and Planetary Science Conference*, p. 1191.

McKenzie, D., Ford, P. G., Liu, F. and Pettengill, G. H. (1992) 'Pancakelike domes on Venus', *Journal of Geophysical Research*. Wiley-Blackwell, 97(E10), p. 15967. doi: 10.1029/92JE01349.

Montserrat, S., Tamburrino, A., Roche, O. and Niño, Y. (2012) 'Pore fluid pressure diffusion in defluidizing granular columns', *Journal of Geophysical Research: Earth Surface*, 117(F2), p. n/a-n/a. doi: 10.1029/2011JF002164.

Moore, H. J., Plaut, J. J., Schenk, P. M. and Head, J. W. (1992) 'An unusual volcano on Venus', *Journal of Geophysical Research*, 97(E8), p. 13479. doi: 10.1029/92JE00957.

Moore, H. J., Schenk, P. M., Plaut, J. J. and Weitz, C. M. (1992) 'An Explosive Eruption on Venus', in *Abstracts of the Lunar and Planetary Science Conference*, pp. 23–927.

Pitman, E. B. and Long, L. E. (2005) 'A two-fluid model for avalanche and debris flows', in *Philosophical Transactions of the Royal Society A: Mathematical, Physical and Engineering Sciences*. Royal Society, pp. 1573–1601. doi: 10.1098/rsta.2005.1596.

Robin, C., Eissen, J.-P. and Monzier, M. (1995) 'Mafic pyroclastic flows at Santa Maria (Gaua) Volcano, Vanuatu: the caldera formation problem in mainly mafic island arc volcanoes', *Terra Nova*, 7(4), pp. 436–443. doi: 10.1111/j.1365-3121.1995.tb00539.x.

Robin, C., Eissen, J. P. and Monzier, M. (1994) 'Ignimbrites of basaltic andesite and andesite compositions from Tanna, New Hebrides Arc', *Bulletin of Volcanology*. Springer-Verlag, 56(1), pp. 10–22. doi: 10.1007/BF00279725.

Roche, O. (2012) 'Depositional processes and gas pore pressure in pyroclastic flows: An experimental perspective', *Bulletin of Volcanology*. Springer, 74(8), pp. 1807–1820. doi:

949 10.1007/s00445-012-0639-4.
950 Roche, O., Montserrat, S., Niño, Y. and Tamburrino, A. (2008) 'Experimental observations of
951 water-like behavior of initially fluidized, dam break granular flows and their relevance for the
952 propagation of ash-rich pyroclastic flows', *Journal of Geophysical Research*. Blackwell
953 Publishing Ltd, 113(B12), p. B12203. doi: 10.1029/2008JB005664.
954 Rooyakkers, S. M., Stix, J., Berlo, K. and Barker, S. J. (2020) 'Emplacement of unusual rhyolitic
955 to basaltic ignimbrites during collapse of a basalt-dominated caldera: The Halarau{eth}ur
956 eruption, Krafla (Iceland)', *Bulletin of the Geological Society of America*. Geological Society of
957 America, 132(9–10), pp. 1881–1902. doi: 10.1130/B35450.1.
958 Schumacher, R. and Mues-Schumacher, U. (1996) 'The Kizilkaya ignimbrite - An unusual low-
959 aspect-ratio ignimbrite from Cappadocia, central Turkey', *Journal of Volcanology and*
960 *Geothermal Research*. Elsevier, 70(1–2), pp. 107–121. doi: 10.1016/0377-0273(95)00046-1.
961 Self, S. (2006) 'The effects and consequences of very large explosive volcanic eruptions',
962 *Philosophical Transactions of the Royal Society A: Mathematical, Physical and Engineering*
963 *Sciences*. Royal Society, 364(1845), pp. 2073–2097. doi: 10.1098/rsta.2006.1814.
964 Self, S., Goff, F., Gardner, J. N., Wright, J. V. and Kite, W. M. (1986) 'Explosive rhyolitic
965 volcanism in the Jemez Mountains: Vent locations, caldera development and relation to regional
966 structure', *Journal of Geophysical Research*, 91(B2), p. 1779. doi: 10.1029/JB091iB02p01779.
967 Sheridan, M. F. (1979) 'Emplacement of pyroclastic flows: A review', *Geologica l Societ y o f*
968 *Americ a Special Paper 180*.
969 Sheridan, M. F., Stinton, A. J., Patra, A., Pitman, E. B., Bauer, A. and Nichita, C. C. (2005)
970 'Evaluating Titan2D mass-flow model using the 1963 Little Tahoma Peak avalanches, Mount
971 Rainier, Washington', *Journal of Volcanology and Geothermal Research*. Elsevier, 139(1–2), pp.
972 89–102. doi: 10.1016/J.JVOLGEORES.2004.06.011.
973 Smrekar, S. E., Hensley, S., Dyar, M. D., Helbert, J. and the VERITAS Science Team (2016)
974 'VERITAS (Venus Emissivity, Radio Science, InSAR, Topography and Spectroscopy): A
975 proposed Discovery Mission', in *47th Lunar and Planetary Science Conference*, p. abs. 2439.
976 Smrekar, S. E. and Stofan, E. R. (1997) 'Corona formation and heat loss on Venus by coupled
977 upwelling and delamination', *Science*. American Association for the Advancement of Science,
978 277(5330), pp. 1289–1294. doi: 10.1126/science.277.5330.1289.
979 Sparks, R. S. J. (1976) 'Grain size variations in ignimbrites and implications for the transport of

980 pyroclastic flows', *Sedimentology*, 23(2), pp. 147–188. doi: 10.1111/j.1365-
981 3091.1976.tb00045.x.
982 Sparks, R. S. J. (1978) 'Gas release rates from pyroclastic flows: a assessment of the role of
983 fluidisation in their emplacement', *Bulletin Volcanologique*. Springer, 41(1), pp. 1–9. doi:
984 10.1007/BF02597679.
985 Sparks, R. S. J., Self, S. and Walker, G. P. L. (1973) 'Products of ignimbrite eruptions', *Geology*.
986 Geological Society of America, 1(3), pp. 115–118. doi: 10.1130/0091-
987 7613(1973)1<115:POIE>2.0.CO;2.
988 Sparks, S., Self, S., Pyle, D., Oppenheimer, C., Rymer, H. and Grattan, J. (2005) *Super-*
989 *eruptions: global effects and future threats: Report of a Geological Society of London Working*
990 *Group*.
991 Stofan, E. R. (1992) 'Global distribution and characteristics of coronae and related features on
992 Venus: implications for origin and relation to mantle processes', *Journal of Geophysical*
993 *Research*, 97(E8). doi: 10.1029/92je01314.
994 Streck, M. J. and Grunder, A. L. (1995) 'Crystallization and welding variations in a widespread
995 ignimbrite sheet; the Rattlesnake Tuff, eastern Oregon, USA', *Bulletin of Volcanology*. Springer-
996 Verlag, 57(3), pp. 151–169. doi: 10.1007/BF00265035.
997 Sugita, S. and Matsui, T. (1993) 'Are Plinian Type Eruptions Possible on Venus?', in *24th Lunar*
998 *and Planetary Science Conference*. Houston.
999 Surkov, Y. A., Barsukov, V. L., Moskalyeva, L. P., Kharyukova, V. P. and Kemurdzhian, A. L.
1000 (1984) 'New data on the composition, structure, and properties of Venus rock obtained by
1001 Venera 13 and Venera 14', *Journal of Geophysical Research*, 89(S02), p. B393. doi:
1002 10.1029/JB089iS02p0B393.
1003 Surkov, Y. A., Moskalyeva, L. P., Shcheglov, O. P., Kharyukova, V. P., Manvelyan, O. S.,
1004 Kirichenko, V. S. and Dudin, A. D. (1983) 'Determination of the elemental composition of rocks
1005 on Venus by Venera 13 and Venera 14 (preliminary results)', *Journal of Geophysical Research:*
1006 *Solid Earth*, 88(S02), pp. A481–A493. doi: 10.1029/JB088IS02P0A481.
1007 Thornhill, G. D. (1993) 'Theoretical modeling of eruption plumes on Venus', *Journal of*
1008 *Geophysical Research: Planets*. Wiley-Blackwell, 98(E5), pp. 9107–9111. doi:
1009 10.1029/93JE00255.
1010 Toro, E. F. (2009) *Riemann solvers and numerical methods for fluid dynamics: A practical*

introduction, *Riemann Solvers and Numerical Methods for Fluid Dynamics: A Practical Introduction*. Springer Berlin Heidelberg. doi: 10.1007/b79761.

Toro, E. F., Millington, R. C. and Nejad, L. A. M. (2001) 'Towards Very High Order Godunov Schemes', in *Godunov Methods*. Springer US, pp. 907–940. doi: 10.1007/978-1-4615-0663-8_87.

Walker, G. P. L., Heming, R. F. and Wilson, C. J. N. (1980) 'Low-aspect ratio ignimbrites', *Nature*, pp. 286–287. doi: 10.1038/283286a0.

Walker, G. P. L., Wilson, C. J. N. and Froggatt, P. C. (1980) 'Fines-depleted ignimbrite in New Zealand - The product of a turbulent pyroclastic flow', *Geology*. Geological Society of America, 8(5), pp. 245–249. doi: 10.1130/0091-7613(1980)8<245:FIINZT>2.0.CO;2.

Watkins, S. D., Giordano, G., Cas, R. A. F. and De Rita, D. (2002) 'Emplacement processes of the mafic Villa Senni Eruption Unit (VSEU) ignimbrite succession, Colli Albani volcano, Italy', *Journal of Volcanology and Geothermal Research*. Elsevier, 118(1–2), pp. 173–203. doi: 10.1016/S0377-0273(02)00256-1.

White, J. D. L. (2000) 'Subaqueous eruption-fed density currents and their deposits', *Precambrian Research*, 101(2–4), pp. 87–109. doi: 10.1016/S0301-9268(99)00096-0.

Wilson, C. J. N. (1984) 'The role of fluidization in the emplacement of pyroclastic flows, 2: Experimental results and their interpretation', *Journal of Volcanology and Geothermal Research*. doi: 10.1016/0377-0273(84)90066-0.

Wilson, C. J. N. (1985) 'The Taupo Eruption, New Zealand II. The Taupo ignimbrite', *Philosophical Transactions of the Royal Society A: Mathematical, Physical and Engineering Sciences*. Royal Society Publishing, 314(1529), pp. 229–310. doi: 10.1098/rsta.1985.0020.

Wilson, C. J. N. (2008) 'Supereruptions and supervolcanoes: Processes and products', *Elements*. GeoScienceWorld, 4(1), pp. 29–34. doi: 10.2113/GSELEMENTS.4.1.29.

Wilson, L. and Head, J. W. (1981) 'Morphology and rheology of pyroclastic (of Mount St. Helens) flows and their deposits and guidelines for future observations', *U.S. Geological Survey Professional Paper*, 1250, pp. 143–155. doi: 10.3133/pp1250.

Wilson, L. and Head, J. W. (1983) 'A comparison of volcanic eruption processes on Earth, Moon, Mars, Io and Venus', *Nature*. Nature Publishing Group, 302(5910), pp. 663–669. doi: 10.1038/302663a0.